

Individual overtopping volumes, water layer thickness and front velocities at rubble mound breakwaters with a smooth crest in shallow water

de Ridder, Menno P.; van Kester, Dennis C.P.; Mares-Nasarre, Patricia; van Gent, Marcel R.A.

DOI

[10.1016/j.coastaleng.2025.104701](https://doi.org/10.1016/j.coastaleng.2025.104701)

Publication date

2025

Document Version

Final published version

Published in

Coastal Engineering

Citation (APA)

de Ridder, M. P., van Kester, D. C. P., Mares-Nasarre, P., & van Gent, M. R. A. (2025). Individual overtopping volumes, water layer thickness and front velocities at rubble mound breakwaters with a smooth crest in shallow water. *Coastal Engineering*, 198, Article 104701. <https://doi.org/10.1016/j.coastaleng.2025.104701>

Important note

To cite this publication, please use the final published version (if applicable). Please check the document version above.

Copyright


Other than for strictly personal use, it is not permitted to download, forward or distribute the text or part of it, without the consent of the author(s) and/or copyright holder(s), unless the work is under an open content license such as Creative Commons.

Takedown policy

Please contact us and provide details if you believe this document breaches copyrights. We will remove access to the work immediately and investigate your claim.



Individual overtopping volumes, water layer thickness and front velocities at rubble mound breakwaters with a smooth crest in shallow water

Menno P. de Ridder ^{a,b} ,* , Dennis C.P. van Kester ^{c,b} , Patricia Mares-Nasarre ^b , Marcel R.A. van Gent ^{a,b}

^a Deltares, Department of Coastal Structures and Waves, The Netherlands

^b Delft University of Technology, Department of Hydraulic Engineering, Delft, The Netherlands

^c Van Oord, Rotterdam, The Netherlands

ARTICLE INFO

Keywords:

Wave overtopping
Shallow foreshore
Rubble mound breakwater
Individual overtopping volumes
Water layer thickness
Flow depth
Front velocity
Individual overtopping distribution

ABSTRACT

Individual overtopping events are important variables when designing a coastal structure as they can deviate significantly from the mean overtopping discharge. Thus, in this study, extreme overtopping events at rubble mound structures with a smooth crest in shallow water have been studied. Both the water layer thickness (flow depth), front velocity and individual overtopping volumes are measured in a wave flume for typical coastal structures with a smooth crest in shallow water for a large range of hydraulic conditions and three different foreshore slopes. An analysis of the individual overtopping volumes shows that the largest individual overtopping volumes arise from short waves that travel on the crest of a low-frequency wave in shallow water and short waves that travel on top of the trough in deep water. Due to the temporal water level variation caused by the low-frequency waves in shallow water, there are fewer overtopping events compared to deep water conditions with the same non-dimensional overtopping discharge. However, the individual overtopping volumes of these events are larger. To quantify the extreme overtopping variables, an empirical formulation based on the relative crest height and short-wave steepness is proposed for the non-dimensional 2% exceedance water layer thickness, front velocity and individual overtopping volume in terms of incident waves with an R^2 of 0.84, R^2 of 0.55 and R^2 of 0.85 respectively. A further small improvement is found when the low-frequency wave height and 2% exceedance wave height are included, but the added value of this expression does not outweigh the additional wave variables needed for the expression. A log-normal distribution with a constant shape and an expression for the scale of the distribution is proposed to describe the distribution of the individual overtopping volumes in shallow water which accurately captures the distribution (R^2 of 0.90). Compared to most of the current design approach which is based on a cascade of empirical formulations, this is a significant improvement. In addition, the reasonable results for a distribution with a constant shape parameter show that the shape of the distribution does not change significantly for shallow water conditions.

1. Introduction

When designing a coastal structure, the mean overtopping discharge is typically applied to determine the crest height and evaluate breakwater's safety. However, it is known that extreme individual overtopping events, characterized by the water layer thickness, front velocity and individual volumes, are also relevant for a safe and reliable design (e.g. Schüttrumpf and Van Gent, 2003; Mares-Nasarre et al., 2019, 2020; Koosheh et al., 2022, 2024). For the same mean overtopping discharge, the extreme individual overtopping events can deviate significantly (Franco et al., 1995). Therefore, when considering pedestrian safety or the stability of the material behind the structure, it

is relevant to not only assess the mean overtopping discharge but also to verify the extreme water layer thickness, flow velocities, and individual overtopping volumes at the breakwater crest (Bae et al., 2016).

Several approaches exist to compute the extreme individual overtopping events. One could apply numerical models (e.g. Chen et al., 2022), machine learning techniques (e.g. Mares-Nasarre et al., 2021) or empirical formulations (e.g. Mares-Nasarre et al., 2020; Koosheh et al., 2022, 2024). The advantage of an empirical formulation is that it is easily applicable in contrast to numerical models which require more computational time. Moreover, the empirical methods explicitly give the user the relationships between the variables that cannot be easily

* Corresponding author at: Delft University of Technology, Department of Hydraulic Engineering, Delft, The Netherlands.
E-mail address: menno.deridder@deltares.nl (M.P. de Ridder).

retrieved from a machine learning method. Therefore, this study focuses on the empirical formulations of extreme individual overtopping events at rubble mound structures with a smooth crest.

Several formulations exist to describe the extreme water layer thickness and front velocity (e.g. Van Gent, 2002; Schüttrumpf and Van Gent, 2003; Mares-Nasarre et al., 2019; Koosheh et al., 2024). However, most of these formulations are derived for conditions ranging between intermediate water to deep water depths (Koosheh et al., 2024; Mares-Nasarre et al., 2019, for a $H_{m0}/h < 0.31$ and $H_{m0}/h < 0.61$ respectively) or impermeable structures (Van Gent, 2002). These existing formulations are sufficient for coastal structures in deep water but when a shallow foreshore is present in front of a permeable structure limited formulations are available. Moreover, the effects of hydrodynamic processes relevant to wave propagation in shallow water on extreme individual overtopping events are not well understood.

Next to the extreme individual events, also the distribution of the overtopping variables is becoming increasingly important as a probabilistic approach is desired. It is essential to understand the distribution of several variables such as individual overtopping volumes to determine the probability of failure of a coastal structure. Several authors studied the individual volume distribution for conditions with relatively deep water at the toe of the structures and thus, without wave breaking on the foreshore (e.g. Molines et al., 2019, with $H_{m0}/h < 0.3$). Nørgaard et al. (2014) performed experiments in shallow water with $H_{m0}/h < 0.55$. However, a practical formulation to accurately describe the distribution of the individual overtopping volumes with significant wave breaking ($H_{m0}/h > 0.5$) at the foreshore for extremely shallow water is not available.

In this study, the effects of shallow foreshores on the water layer thickness, front velocity and individual overtopping volumes in terms of incident waves during wave overtopping events at rubble mound structures with a smooth crest are systematically studied using physical model experiments. In addition, an empirical expression for the distribution of the individual overtopping volumes in terms of overtopping events is derived for shallow water.

The paper is structured as follows. In Section 2, a literature review is given. In Section 3, the relevant processes and variables for shallow water conditions for wave–structure interaction are described. In Section 4, the physical model experiments are described (see also De Ridder et al., 2024). In Section 5, the effects of the shallow water processes on the overtopping events are addressed. In Section 6, the results for the individual overtopping events are given. In Section 7, the discussion of the results is described. Finally, in Section 8, the conclusions and recommendations are given.

2. Background

2.1. Extreme individual overtopping variables

Cox and Machemehl (1986) derived an expression for the water layer thicknesses over an impermeable structure based on a bore analogy. This was generalized with an expression for different locations at the crest and seaward slope for irregular waves by both Schüttrumpf et al. (2003) and Van Gent (2003). Both Schüttrumpf et al. (2003) and Van Gent (2003) performed physical model experiments to determine the 2% exceedance value of the water layer thickness ($h_{2\%}$) and velocity ($u_{2\%}$) in terms of number of incident waves. Based on a combination of both datasets, Schüttrumpf and Van Gent (2003) derived a formulation for $h_{2\%}$ and $u_{2\%}$ at the seaside of a dike based on the virtual 2% exceedance runup height ($R_{u2\%}$),

$$h_{2\%}(z_a)/H_{m0} = c_h \left(\frac{R_{u2\%} - z_a}{H_{m0}\gamma_f} \right) \quad (1)$$

$$u_{2\%}(z_a)/\sqrt{gH_{m0}} = c_u \sqrt{\frac{R_{u2\%} - z_a}{H_{m0}\gamma_f}} \quad (2)$$

where z_a is the height defined relative from the still water, H_{m0} the significant wave height, g the gravitational acceleration and c_h and c_u are calibration coefficients (see Table 1). The formulations proposed by Schüttrumpf and Van Gent (2003) did not include a roughness factor (γ_f), but in Van Gent (2002) the roughness factor was included. The runup height, $R_{u2\%}$ (see Appendix A), is obtained from the expression given in Van Gent (2001).

Schüttrumpf and Van Gent (2003) also presented an expression for the evolution of the water layer thickness and front velocity along the crest,

$$h_{2\%}(x_c)/h_{2\%}(R_c) = \exp(-c_{c,h}x_c/B) \quad (3)$$

$$u_{2\%}(x_c)/u_{2\%}(R_c) = \exp(-c_{c,u}x_c\mu/h_{2\%}(R_c)) \quad (4)$$

where x_c is the location at the crest, B is the crest width, μ is a friction coefficient (typical values ranging between 0 and 0.1), $h_{2\%}(R_c)$ and $u_{2\%}(R_c)$ are respectively the 2% exceedance water layer thickness and front velocity at the crest and $c_{c,h}$ and $c_{c,u}$ are coefficients. Both Schüttrumpf et al. (2003) and Van Gent (2003) suggested $c_{c,u} = 0.5$, $c_{c,h} = 0.89$ for the data by Schüttrumpf et al. (2003) and $c_{c,u} = 0.4$ for the data by Van Gent (2003). Bosman et al. (2009) suggested that these differences could be caused by slope effects and derived new coefficients based on the slope of the structure (see Table 1). Later, Van der Meer et al. (2010) proposed alternative coefficients for Eqs. (3) and (4) (see Table 1). Van Gent (2003) also presented an expression for the 2% exceedance overtopping volume in terms of incident waves for a sea dike given by,

$$\frac{V_{2\%}}{H_{m0}^2} = c_v \gamma_f^{0.5} \left(\frac{R_{2\%} - R_c}{H_{m0}\gamma_f} \right)^2 \quad (5)$$

where c_v is an coefficient equal to 1, γ_f a roughness factor, γ_{f-c} a roughness factor at the crest and $R_{2\%}$ the 2% exceedance runup calculated with the equation in Van Gent (2001).

Mares-Nasarre et al. (2019) extended the work of Schüttrumpf and Van Gent (2003) to rubble mound breakwaters and found a coefficient of $c_h = 0.52$ for the water layer thickness for a rubble mound structure. Mares-Nasarre et al. (2019) also proposed to use the TAW (2002) formulation, also used in EurOtop (2018), to estimate the $R_{u2\%}$. The results of Mares-Nasarre et al. (2019) were obtained at the middle of the crest and Eq. (3) was used with a coefficient $c_{c,h} = 0.89$. Koosheh et al. (2024) performed experiments with a coastal structure with an impermeable core and found a value of $c_h = 0.24$ where also the TAW (2002) formulation was applied for $R_{u2\%}$. Koosheh et al. (2024) used Eq. (3) with $c_{c,h} = 0.40$. In Table 1, an overview is given for the various coefficients found in the literature with R_c/H_{m0} and H_{m0}/h ranges. However, the applicability of the formulations for rubble mound breakwaters in extremely shallow water has never been verified.

2.2. Individual overtopping volumes

The distribution of individual overtopping volumes in terms of number of overtopping events is also commonly applied and mainly required for probabilistic approaches. The most common distribution in literature to describe the individual overtopping volumes is the 2-parameter Weibull distribution for which the cumulative distribution is given by,

$$F(V_i) = 1 - e^{-(V_i/\lambda)^b} \quad (6)$$

where λ is the scale parameter, b the shape parameter and V_i the individual overtopping volume. To obtain a non-dimensional λ , it is often substituted by $\lambda = A\bar{V}$, where \bar{V} is the mean individual overtopping volume. When the mean of the distribution is set equal to the mean overtopping volume (\bar{V}) a relation between A and b exists,

$$A = \frac{1}{\Gamma(1+1/b)} \quad (7)$$

Table 1

Coefficient for water layer thickness and front velocity for Eqs. (1) and (2). The applied formulation for $R_{u2\%}$, the structure type, the R_c/H_{m0} ranges and the H_{m0}/h ranges are also shown.

| Reference | c_h | c_u | Runup formulation | Structure type | R_c/H_{m0} | H_{m0}/h |
|-----------------------------|----------------------|--------------------|----------------------------|------------------------------|--------------|------------------------|
| Schüttrumpf et al. (2003) | 0.33 | 1.37 | Based on Hunt (1959) | Dike (Smooth impermeable) | 0.0–4.4 | 0.2–1.4 |
| Van Gent (2003) | 0.15 | 1.3 | Eq. (A.1) (Van Gent, 2001) | Dike (Smooth impermeable) | 0.7–2.2 | 0.1–0.3 |
| Bosman et al. (2009) | $0.01/\sin^2 \alpha$ | $0.3/\sin \alpha$ | Unknown | Dike (Smooth impermeable) | 0.0–4.4 | 0.1–1.4 |
| Van der Meer et al. (2010) | 0.13 | $0.35 \cot \alpha$ | Unknown | Dike (Smooth impermeable) | 0.7–2.9 | 0.1–0.3 ^a |
| Mares-Nasarre et al. (2019) | 0.52 | – | Eq. (A.2) (TAW, 2002) | Rubble mound breakwater | 0.80–1.75 | 0.29–0.61 ^b |
| Koosheh et al. (2024) | 0.24 | – | Eq. (A.2) (TAW, 2002) | Revetment (impermeable core) | 0.75–2.36 | 0.15–0.31 |

^a Combination of data from Van Gent (2003) and Schüttrumpf et al. (2003).

^b Rocks 2 layer.

where Γ is the gamma function. A large shape parameter ($b > 3$) means that the distribution is more or less uniform distributed and thus, most of the overtopping waves contribute to the total overtopping volume. A low shape parameter ($b < 0.75$) results in a distribution with only a few overtopping events contributing to the total volume. Various authors studied the influence of wave characteristics on the shape parameter (see Table 2). For example, Franco et al. (1995) suggested applying the Weibull distribution with a $b = 0.72$ to describe the probability of individual overtopping volumes for rubble mound breakwater. Victor et al. (2012) conducted small-scale experiments and showed that the b is related to the relative crest height and structure slope for smooth steep slopes. Hughes et al. (2012) reanalyzed existing data focusing on extreme individual overtopping volumes and found a relationship between b and R_c/H_{m0} for smooth slopes. Nørgaard et al. (2014) performed experiments in depth-limited wave conditions for a rubble mound breakwater ($H_{m0}/h > 0.55$) and derived an expression based on the water depth and the average of the 10 largest waves. Moreover, several authors made a relationship between q and b (Zanutigh et al., 2014; Molines et al., 2019; Mares-Nasarre et al., 2020). Later Mares-Nasarre et al. (2024) suggested applying the log-normal distribution (see Appendix C for the definition of the distribution) to describe the individual overtopping volumes instead of the Weibull distribution, where the μ_V , the mean of the variable's natural logarithm, is given by,

$$\mu_V = 0.6 \left(\frac{R_c}{H_{m0}} \right)^{-1} - 30s_{m-1,0} \quad (8)$$

and the shape parameter (s) is given by,

$$s = -8m - 0.2 \left(\frac{R_c}{H_{m0}} \right) - 6s_{m-1,0} \quad (9)$$

where m is the foreshore slope, R_c is the free board, H_{m0} is the wave height and $s_{m-1,0}$ is the wave steepness. An overview of all the expressions for b in literature is given in Table 2, which shows that an expression for rubble mound breakwaters validated for (extreme) shallow water is lacking.

The individual overtopping distribution is given in terms of overtopping waves. The Weibull plotting position formula can be used to transform the probabilities in terms of overtopping events to incident waves,

$$F(V_i) = 1 - \frac{i}{N_{ov} + 1} \quad (10)$$

where i is the rank of the individual volume and N_{ov} the number of overtopping waves.

Next to the distribution of the individual overtopping volumes also the probability of overtopping (P_{ov}) is an important variable as it is needed to transform the probability of individual overtopping volumes to a probability in terms of incident waves. Besley (1998) proposed a function, applicable for complex structures, related to the mean

overtopping discharge to predict the probability of overtopping,

$$P_{ov} = \begin{cases} 55.4(q^*)^{0.634} & \text{for } 0 < q^* < 8 \times 10^{-4} \\ 2.5(q^*)^{0.199} & \text{for } 8 \times 10^{-4} < q^* < 10^{-2} \\ 1 & \text{for } q^* > 10^{-2} \end{cases} \quad (11)$$

where q^* is the non-dimensional mean overtopping discharge. Next to the expression given by Besley (1998) the following expression is given in the EurOtop (2018) manual,

$$P_{ov} = \exp \left(- \left(\frac{1}{\chi} \frac{R_c}{H_{m0}} \right)^2 \right) \quad (12)$$

where χ is given by,

$$\chi = 1/\sqrt{-\ln(0.02)} \quad (13)$$

More recently, Molines et al. (2019) and Mares-Nasarre et al. (2020) proposed a function related to the overtopping discharge. The deep water formulation given in Molines et al. (2019) is shown in Eq. (14).

$$P_{ov} = 480 \left(\frac{q}{gT_{m01}H_{m0}} \right)^{0.8} \quad (14)$$

The depth-limited formulation is given by Mares-Nasarre et al. (2020) as,

$$P_{ov} = \exp \left(- \frac{0.1}{\left(\frac{q}{gT_{m01}H_{m0}} \right)^{0.3}} \right) \quad (15)$$

where T_{m01} is the mean absolute wave period, q the mean overtopping discharge and H_{m0} the wave height.

3. Shallow water processes

The hydrodynamics in shallow water are different than in deep water conditions. In De Ridder et al. (2024) the effects of a shallow foreshore on the mean overtopping discharge over a rubble mound structure with a smooth crest were analysed. It was found that the most important variables describing the mean overtopping discharge are the short-wave steepness ($s_{m-1,0,HF}$, representing the energy of the short waves), relative crest height (R_c/H_{m0}) and low-frequency wave height ($H_{m0,LF}$, see Fig. 1 for an overview and the definitions of the variables).

An important process in shallow water is depth-induced wave breaking, resulting in a non-Rayleigh distributed wave field (e.g. Battjes and Groenendijk, 2000). It is expected that this will reduce the water layer thickness (h_i) and individual overtopping volumes (V_i , see Fig. 1 for the definitions), particularly for high relative crest freeboards (R_c) where mainly the largest waves overtop the structure. Nørgaard et al. (2014) studied the effect of a shallow water depth on the individual overtopping volumes and concluded that individual overtopping volumes are more uniformly distributed and proposed 2-parameter Weibull distribution with a b dependent on $H_{m0}/H_{1/10}$.

Table 2

Formulations for the Weibull shape parameter (b) describing the distribution of individual overtopping volumes. The maximum value of H_{m0}/h is also shown.

| Reference | H_{m0}/h | Weibull shape parameter (b) |
|------------------------------|-------------------|--|
| Franco et al. (1995) | $H_{m0}/h < 0.33$ | $b = 0.75$ |
| Victor et al. (2012) | $H_{m0}/h < 0.13$ | $b = \exp(-2.0R_c/H_{m0}) + 0.56 + 0.15 \cot \alpha$ |
| Hughes et al. (2012) | Unspecified | $b = \exp(-0.6R_c/H_{m0})^{1.8} + 0.64$ |
| Nørgaard et al. (2014) | $H_{m0}/h < 0.55$ | $b = \begin{cases} 0.75 & \text{for } H_{m0}/H_{1/10} < 0.848 \text{ or } H_{m0}/h < 0.2 \\ -6.1 + 8.08H_{m0}/H_{1/10} & \text{for } H_{m0}/H_{1/10} > 0.848 \text{ or } H_{m0}/h > 0.2 \end{cases}$ |
| Molines et al. (2019) | $H_{m0}/h < 0.30$ | $b = 0.63 + 1.15 \exp(-3 \times 10^5 \frac{q}{gH_{m0}T_m})$ |
| Mares-Nassarre et al. (2020) | $H_{m0}/h < 0.61$ | $b = 0.8 + \exp(-2 \times 10^5 \frac{q}{gH_{m0}T_m})$ |

Next to depth-induced wave breaking, the non-linear wave interaction becomes dominant (e.g. Longuet-Higgins and Stewart, 1962; Hasselmann, 1962) by transferring energy within the spectrum. The energy at the lower frequencies is mainly important for extreme individual overtopping events because these waves do not break and result in a temporary increase in the water level (illustrated as η_{LF} in Fig. 1). It is shown in De Ridder et al. (2024) that the 2% exceedance wave height ($H_{2\%}$) can become relatively large compared to the short wave height ($H_{m0,HF}$) because of these low-frequency waves. It is therefore hypothesized that the low-frequency waves could affect the extreme individual overtopping events because the extreme individual overtopping will most likely be related to the 2% exceedance wave height. This effect is more pronounced for long-period wave conditions because the energy transfer to lower frequencies is larger. In contrast to depth-induced wave breaking, this effect will result in larger individual overtopping volumes and water layer thickness because the water level is temporarily increased.

It is hypothesized that the water depth itself could affect the individual overtopping volumes. The individual overtopping volumes can be described by the integral of the water layer thickness times the front velocity ($V_i = \int u(t)h(t)dt$). For shallow water conditions, the front velocity (u_i) will be lower because the wave celerity is lower in shallow water and only depends on the water depth.

Van Gent (1999) characterized the effects of wave breaking and the importance of low-frequency on shallow foreshores with the ratio of the deep water wave height ($H_{m0,deep}$) over the local water depth (h). De Ridder et al. (2024) showed that these ranges apply well to the various transitions in relevant wave variables. For $H_{m0,deep}/h < 0.4$ the conditions can be characterized as ‘deep’ with limited wave breaking. For $0.4 < H_{m0,deep}/h < 1$ (intermediate) there is some wave breaking and energy transfer to low-frequencies. In shallow water ($1 < H_{m0,deep}/h < 3$) severe wave breaking occurs and large amounts of energy are present at the lower frequencies. For $H_{m0,deep}/h > 3$ the conditions can be characterized as ‘very shallow’, where mainly energy at lower frequencies is present.

4. Physical model tests

4.1. Model set-up

Here, experiments by De Ridder et al. (2024) are used with focus on individual overtopping events characterized by water layer thicknesses, flow velocities and individual overtopping volumes, rather than on mean overtopping discharges.

Three different foreshores (A, B and C series) were tested with a foreshore slope of 1:100, 1:50 and 1:20 (see Fig. 2). A transition slope of 1:10 was applied for the 1:100 foreshore until a height of 0.2 m. At the end of the foreshore at an elevation of 0.5 m, a rubble mound breakwater was constructed with a slope (α) of $\cot \alpha = 2$ (see Fig. 3). A double-layer rock armour layer with a $D_{n50} = 23.9$ mm was applied with a core of a $D_{n50} = 8.5$ mm. The porosity of the structure was approximately 0.4. To avoid creating an unrealistic structure for milder wave conditions by using large stones stable for the most extreme tests, the stones were glued together to prevent the armour layer from

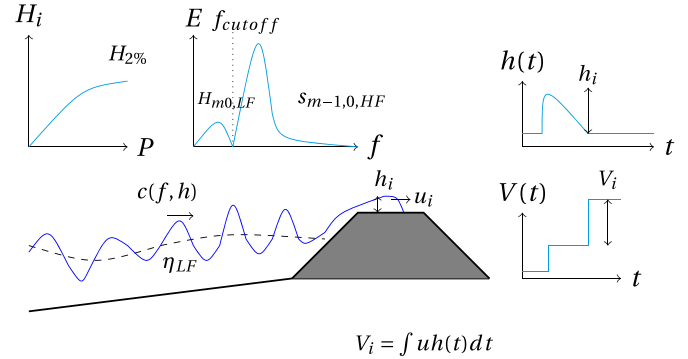


Fig. 1. Shallow water physics related to wave overtopping and an illustration of the definitions applied in this study. An illustrative wave spectrum is shown with the definitions of the $H_{m0,LF}$ and $s_{m-1,0,HF}$. At the crest, the definitions of the water layer thickness and front velocity are shown ($h_{2\%}$ and $u_{2\%}$).

deforming. This did not affect the permeability nor the roughness because only the contact points of the stones are glued together. In Table 1 of De Ridder et al. (2024) the coordinates of the features in the wave flume are given. The offshore water depth (h_{deep}) was varied between 0.55 m and 0.9 m. The crest level (h_{crest}) was changed for each water level to obtain overtopping variables in realistic ranges.

To accurately measure the water layer thickness and front velocities, the flume was split into two parts at the structure’s location. On one side the crest was wider ($B = 0.5$ m) to measure the water layer thickness. The other side of the flume had a narrower crest ($B = 0.1$ m) and was used to measure the individual overtopping volumes. The experiments were repeated with the same wave conditions, but without the structure to obtain the incident waves (calibration tests).

The water layer thickness was measured with four water layer thickness instruments (wire resistance gauges) at the crest. The distance between the water layer thickness instruments was 0.1 m (see also Fig. 3). The incident waves were obtained from two sets of wave gauges. Close to the model, the wave gauge Set 2 contained 7 wave gauges (31.14 m from the wave maker) while in deep water, Set 1 contained 4 wave gauges (6.5 m from the wave maker). During these calibration tests, wave gauge Set 2 was moved to the location of the structure. The overtopping volume is measured with two wave gauges in the overtopping box.

4.2. Test programme

The test programme consisted of irregular wave conditions with approximately 1000 waves generated from a JONSWAP spectrum. Variations in the offshore wave height ($H_{m0,deep}$), offshore wave steepness ($s_{m-1,0,deep}$, based on deep water wave length), freeboard (R_c) and water depth (h_{deep}) were applied (see Table 3). In addition, these variations in wave conditions were applied to three different foreshores. A selection of the tested conditions with the 1:100 foreshore slope were repeated with the 1:20 and 1:50 foreshore because the hydrodynamics at the toe did not change significantly compared to the conditions obtained

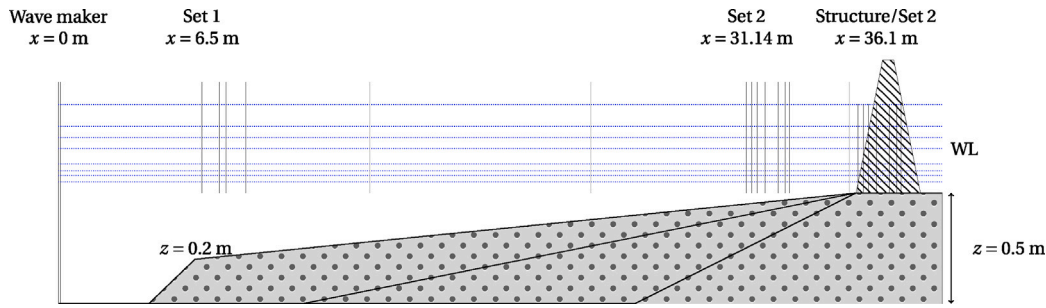


Fig. 2. Schematic overview of model Layout A, B and C. Wave gauges part of a set are shown in black. The coordinates of the wave gauges correspond to the first wave gauge of the set. The gray instruments represent individual wave gauges. Note that the scale is distorted to visualize the layout. The position of wave gauge Set 2 is shown both at the location and during the calibration tests and the test with the breakerwater.

Source: Figure obtained from De Ridder et al. (2024).

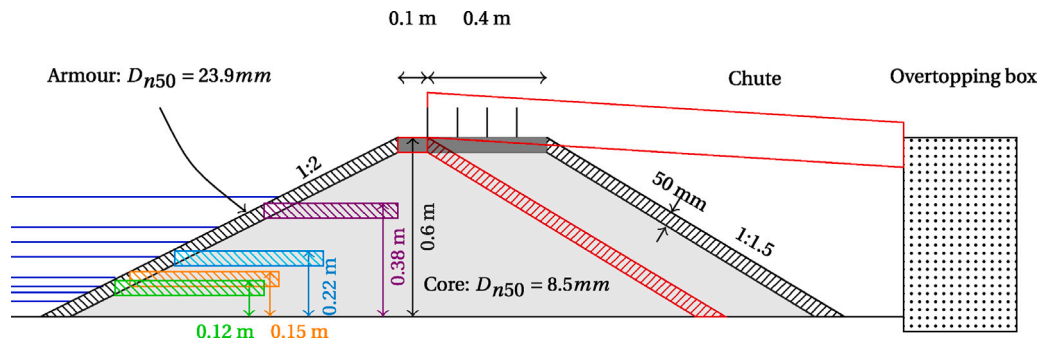


Fig. 3. Cross section of the rubble mound breakwaters. The geometry in red shows the side with the overtopping box and the geometry shown in black is at the side with the longer crest element to measure the water layer thickness. The crest levels of the various configurations are shown in colours (green, orange, cyan, violet and black). The tested water levels are shown in blue.

Source: Figure obtained from De Ridder et al. (2024).

from the 1:100 foreshore slope. In total 144 tests were performed (excluding the calibration tests): 24 tests with a 1:20 foreshore, 39 tests with a 1:50 foreshore and 81 with a 1:100 foreshore. In Table 3 the (incident) variable ranges are given based on wave gauge Set 2. Note that the water depth (h) is defined at the structure's location at the same location where the wave conditions are measured.

As Froude scaling is used as a scaling law, both the Reynold ($Re = \rho u L / \nu$) and Weber number ($We = \rho L u^2 / \sigma$) were verified. Using the $h_{2\%}$ and $u_{2\%}$ as characteristic length (L) and velocity (u) scale and a density of $\rho = 1000 \text{ kg/m}^3$, surface tension of $\sigma = 0.072 \text{ N/m}$ and kinematic viscosity of $\nu = 10^{-6} \text{ m}^2/\text{s}$ this leads to a Re ranging between 2×10^6 – 6×10^8 and a We between 18–2520 showing that surface tension effects are not significant and that the flow is turbulent (e.g. see EurOtop, 2018, for the critical values).

4.3. Analysis of measurements

4.3.1. Incident waves

The incident wave variables are computed based on the time series from wave gauge Set 2 during the calibration tests. It was observed that the very nonlinear (breaking) waves cannot be accurately decomposed into the incident and reflected signals for the extreme shallow water conditions. Therefore, the incident waves were obtained from the measured high-passed signal from the calibration tests. Low-frequencies presented larger reflection coefficients during the calibration tests, so the incident signal was computed with the decomposition approach described in De Ridder et al. (2023) based on the theory in Røge Eldrup and Lykke Andersen (2019). This means that the effect of the reflections on the incident waves is not included in the incident time series and that incident waves are obtained at the location of the structure. This is preferred for deriving a design formulation because practitioners typically obtain incident wave conditions in shallow water from numerical

models which do not include the structure (also common in literature, e.g., Mares-Nasarre et al., 2020; Herrera et al., 2017, for individual events and hydraulic stability respectively).

In this study the spectral variables ($H_{m0} = \sqrt{4m_0}$ and $T_{m-1,0} = m_{-1}/m_0$) are computed based on the spectral moment $m_n = \int_{\Delta f}^{f_{max}} f^n E(f) df$. The entire frequency range is considered for H_{m0} and $T_{m-1,0}$. To distinguish between the short and long waves, both the wave height and spectral period are also computed for the high and low passed signals with a cut-off frequency of the peak frequency (f_p) in deep water divided by 1.5 (see De Ridder et al., 2024). For practical applications, where the peak frequency is not always well defined, it is recommended to determine the cutoff frequency based on the spectral period, which would result in $f_{cutoff} = 0.60/T_{m-1,0}$ given the relation between T_p and $T_{m-1,0}$ in deep water for a JONSWAP spectrum. Moreover, the 2% exceedance wave height ($H_{2\%}$), wave asymmetry (A_s) and wave skewness (S_k) are computed based on the incident time series.

4.3.2. Water layer thickness

The individual water layer thickness events (h_i) are obtained with a peak detection method (see also Panel C of Fig. 4). This method defines the peaks based on a threshold and a minimum period between the peaks. A threshold of 0.002 m is applied to detect the peaks with a minimum period of 0.7 s. The water layer thickness (h_i) is then defined as the maximum value in an overtopping event (see Fig. 3 for the location of the instruments). To obtain a robust estimate of the water layer thickness, the mean signal, corrected for the phase shift, over instruments 2 and 3 is applied as the final water layer signal. This water layer thickness signal corresponds with the middle of the crest.

4.3.3. Front velocity

Two types of front velocities are computed. An average front velocity (\bar{u}) for the entire test is computed based on the required time shift

Table 3

Variables range of test programme (obtained from De Ridder et al. (2024)). Wave gauge Set two (toe of the structure) was used to determine the incident wave variables. The water depth (h) is defined at the location of the structure ($x = 36.1$ m).

| Variable | Symbol | Values/Ranges |
|---|--------------------|---|
| Target offshore wave height (m) | $H_{m0,target}$ | 0.1, 0.15, 0.2 and 0.25 |
| Target offshore wave steepness (-) | $S_{m-1.0,target}$ | 0.015, 0.025 and 0.04 |
| Offshore water depth (m) | h_{deep} | 0.90, 0.80, 0.70, 0.75, 0.60, 0.63, 0.55, 0.58 and 0.55 |
| Foreshore slope (-) | m | 1/100, 1/50 and 1/20 |
| Seaward slope (-) | $\cot \alpha$ | 2 |
| Armour stone diameter (m) | D_{n50} | 0.023 |
| Water depth (m) | h | 0.05–0.4 |
| Incident wave height (m) | H_{m0} | 0.03–0.21 |
| Incident low-frequency wave height (m) | $H_{m0,LF}$ | 0.01–0.06 |
| Incident high-frequency wave height (m) | $H_{m0,HF}$ | 0.02–0.20 |
| Incident spectral period (s) | $T_{m-1.0}$ | 1.14–7.17 |
| Incident high-frequency spectral period (s) | $T_{m-1.0,HF}$ | 0.75–2.42 |
| Wave steepness (-) | $S_{m-1.0}$ | 0.001–0.040 |
| Short-wave steepness (-) | $S_{m-1.0,HF}$ | 0.004–0.047 |
| Iribarren number (-) | $\xi_{m-1.0}$ | 0.05–1.11 |
| Freeboard (m) | R_c | 0.12–0.6 |
| Foreshore slope (-) | m | 1/100,1/50,1/20 |
| Non-dimensional freeboard (-) | R_c/H_{m0} | 0.80–3.72 |
| Non-dimensional stone diameter (-) | D_{n50}/H_{m0} | 0.12–0.89 |
| Relative low-frequency wave height (-) | $H_{m0,LF}/H_{m0}$ | 0.10–0.81 |
| Relative water depth (-) | h/H_{m0} | 0.57–4.95 |
| Relative water depth (offshore wave height) (-) | $h/H_{m0,deep}$ | 0.23–4.59 |

(Δt) to obtain the highest correlation of the water layer thickness signal ($\rho(h_0(t), h_j(t - \Delta t))$) between two instruments, $h_0(t)$ and $h_j(t)$. The mean time shift for the 3 possible distances divided by the spacing between the instruments (Δx_j) results in the mean front velocity,

$$\bar{u} = \frac{1}{3} \sum_j \frac{\Delta t (\arg\max (\rho(h_0(t), h_j(t - \Delta t))))}{\Delta x_j} \quad (16)$$

Next to the mean front velocity, the individual front velocities (u_i) are determined. The same approach is applied but to a time slice of the time series around a single event. A time slice is defined as 0.5 s before the peak of the water layer thickness till 0.5 s after the peak of the water layer thickness.

4.3.4. Individual overtopping volumes

The individual overtopping volumes are estimated based on the water layer thickness and front velocities, as in the overtopping box some cases with multiple overtopping events close to each other are captured as one event (see Panel B and C of Fig. 4). When two events happen close to each other or when the volume is relatively small, it is impossible to determine the volume of these events based on the overtopping box. On average the number of overtopping events obtained from the water layer thickness signal is 9.3 times larger compared to the events obtained from the overtopping box. By assuming a constant front velocity for a single overtopping event, it is possible to compute the volume as,

$$V_i = c_V u_i \int_{t_0}^{t_1} h_{layer}(t) dt \quad (17)$$

where V_i is the overtopping volume for event i , u_i the front velocity of event i , c_V a coefficient, h_{layer} the water layer thickness time series and t_0 and t_1 are the boundaries of the event around t . Based on visual inspection a value of 0.5 s is used for t_0 and a value of 0.7 s is used for t_1 .

This method is validated by comparing the total volume from the overtopping box with the total volume obtained with the proposed method. Based on this analysis it is observed that this method systematically overestimates the volumes with a c_V of 1 (see Appendix B). A reason for this overestimation could be the fact that a constant front velocity is assumed, whereas, in reality, the velocity will decrease within the event. In addition, some air may be present in the water layer thickness that does not affect the volume in the overtopping box. To correct for this effect the obtained volumes are multiplied with a correction factor $c_V = 0.52$, which results in a good agreement

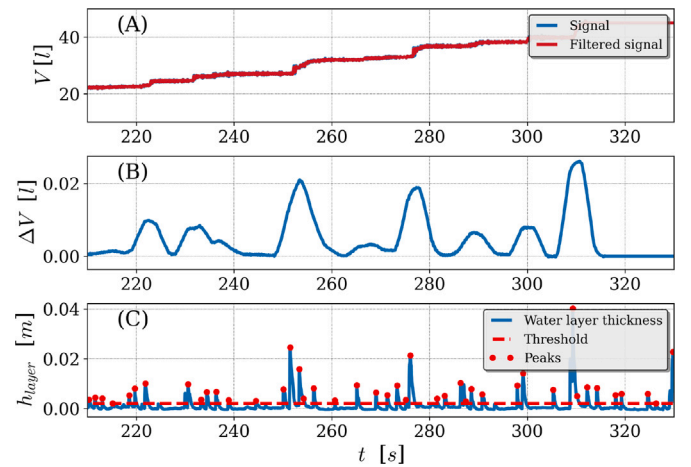


Fig. 4. Cumulative overtopping volume from the overtopping box (Panel A), the derivative of the overtopping box signal (Panel B) and the water layer thickness (Panel C). The applied threshold to determine the water layer thickness event is shown with a red dashed line in Panel C. The detected peaks are shown with red markers. In Panel A, both the raw signal and the filtered signal (with a moving average) are shown for the cumulative overtopping volume.

between the volume in the overtopping box and the proposed method (see Appendix B). This correction factor is the mean correction factor when the total volumes for all relevant experiments are compared to the total volume obtained with Eq. (17). Note that this correction is dependent on the model setup and therefore not generally applicable but only valid for this dataset.

4.3.5. Extreme individual overtopping variables

The extreme individual overtopping variables are normalized by the wave height (H_{m0}), shallow water celerity (\sqrt{gh}) and the squared wave height (H_{m0}^2) for $h_{2\%}$, $u_{2\%}$ and $V_{2\%}$ respectively. The variables are evaluated at the middle of the crest at a distance of 0.25 m from the start of the crest. The 2% exceedance value is considered for each variable as this value is statistically more reliable than the maximum value but still represents the tail of the distribution. Moreover, the definition of the maximum overtopping volume is not clear as it depends on the number of waves and the number of events. For tests with a limited number

of overtopping events, the 2% exceedance value cannot accurately be reliably determined. Thus, only tests with at least 50 overtopping events (5% of the number of incident waves) and a non-dimensional mean overtopping discharge larger than 10^{-5} are considered for the extreme individual overtopping variables. Since the very low water layer thickness event cannot be accurately measured, a threshold slightly higher than typically applied 10^{-6} is used. Also, such low values may be outside the relevant range of practical applications. For the analysis of the distribution of the individual overtopping volumes only tests with at least 75 overtopping events are considered to accurately determine the shape of the distribution.

4.4. Error metrics

The error metrics used in this study are the root-mean-square-error (RMSE), root-mean-square-logarithmic-error (RMSLE) and the adjusted coefficient of determination. The definition of the RMSE and RMSLE are given by Eqs. (18) and (19),

$$RMSE = \sqrt{\left(\frac{1}{N} \sum_{i=1}^N (x_i - y_i)^2\right)} \quad (18)$$

$$RMSLE = \sqrt{\left(\frac{1}{N} \sum_{i=1}^N (\log(x_i + 1) - \log(y_i + 1))^2\right)} \quad (19)$$

where x_i is the estimation, y_i the observation and N the number of observations. For the water layer thickness and front velocities, the RMSE is used while for the individual overtopping volumes, RMSLE is used. Next to RMSE and RMSLE, the adjusted coefficient of determination (R_{adj}^2) is computed as,

$$R_{adj}^2 = 1 - (1 - R^2) \frac{N - 1}{N - 1 - N_p} \quad (20)$$

with R^2 given by,

$$R^2 = 1 - \frac{\sum_{i=1}^N (x_i - y_i)^2}{\sum_{i=1}^N (y_i - \langle y \rangle)^2} \quad (21)$$

where N the number of observations, N_p the number of explanatory variables and $\langle \rangle$ the mean operator. Thus, R_{adj}^2 also takes complexity of the proposed model into account. Moreover, the R_{adj}^2 shows the scatter in a normalized way making it possible to compare the accuracy of various models.

5. Effect of low-frequency waves on individual overtopping volumes

The low-frequency wave height ($H_{m0,LF}$) becomes very important in shallow water. To demonstrate the effect of $H_{m0,LF}$ on individual overtopping volumes (V_i), they are related to the phase of the low-frequency wave. In Panel A and B of Fig. 5, all observed non-dimensional individual overtopping volumes (V_i/H_{m0}^2) are plotted as a function of the free surface level elevation of the low-frequency wave at the moment the overtopping event occurred (η_{LF}). The low-frequency wave signal is obtained through a low-band filter with a cutoff frequency of 0.5 times the peak frequency of the result from the calibration test. The free surface level elevation of the low-frequency wave is normalized with the low-frequency wave height ($H_{m0,LF}$) to be able to compare all test results. This analysis is done both for conditions without severe wave breaking ($H_{m0}/h < 0.5$) and conditions with wave breaking ($H_{m0}/h > 0.5$). Note that this threshold differs slightly from the threshold proposed in Section 3 but with the threshold of 0.5 the number of data points for conditions without severe wave breaking is significantly larger than with 0.4 making the results more reliable.

This analysis reveals that in deep water most of the overtopping events are caused by short waves which travel in the trough of the low-frequency waves as the mean of distribution occurs at a negative low-frequency surface elevation (Panel C of Fig. 5). Moreover, for

decreasing $\eta_{LF}/H_{m0,LF}$, V_i/H_{m0}^2 seems to increase (Panel A of Fig. 5). This is in agreement with the theory of bound long waves where the short wave groups are out-of-phase with the bound long waves (e.g. Janssen et al., 2003). In shallow water, the opposite behaviour is observed. When short waves break, the low-frequency waves become free waves breaking that correlation. However, high short waves can only exist on top of the crest of the low-frequency wave (otherwise wave breaking would occur) resulting in a positive correlation between the phase of the low-frequency wave and the short waves. This also affects the individual overtopping volumes. The largest V_i/H_{m0}^2 occurs for short waves travelling at the crest of a low-frequency wave in shallow water (Panel B of Fig. 5). The distribution of the overtopping events seems to be located around zero $\eta_{LF}/H_{m0,LF}$ for shallow water (Panel D of Fig. 5). The same analysis is also performed for the non-dimensional water layer thickness and front velocities (see Appendix D) where it is concluded that the same principles also hold for u_i/\sqrt{gh} and h_i/H_{m0} .

The non-equally distributed V_i/H_{m0}^2 over the phase of the low-frequency wave also explains part of the findings in De Ridder et al. (2024) for the mean overtopping discharge. If an exponential increase of the overtopping volume as a function of the freeboard is assumed, this would lead to the total overtopping volume being larger for a signal with a slowly varying water level compared to the situation without this slowly varying water level and thus, an effect on the mean overtopping discharge.

To further study this behaviour the fraction of overtopping waves (P_{ov}) is also analysed. Based on the previous findings, it would be expected that there will be fewer overtopping events for conditions with a large amount of energy at the lower frequencies. Due to the slowly varying water level, there will be moments when the water level is too low for the short waves to overtop the structure. This is also found in the observations in this study (see Panel A in Fig. 6). For the same mean overtopping discharge, the conditions with fewer low-frequency waves result in significantly higher fraction of overtopping events (P_{ov}) compared to the same mean overtopping discharge but with more energy at the low-frequency waves.

If the fraction of overtopping events changes but the mean overtopping wave does not change, the individual overtopping volumes must be different. This is visible in Panel B of Fig. 6 where the fraction between the mean individual overtopping volume and the 2% exceedance volume is shown. It appears that this fraction is also dependent on the non-dimensional overtopping discharge itself. This is also found by other authors (e.g. Victor et al., 2012; Hughes et al., 2012) who related the b of the individual volume distribution to the relative crest height. A lower non-dimensional overtopping discharge results in a higher relative 2% exceedance volume. Also, an effect of the low-frequency wave height is visible. For the same non-dimensional overtopping discharge, the relative 2% exceedance volume is larger for conditions with more energy at the lower frequencies. Thus, for conditions with more energy at the lower frequencies, the fraction of overtopping waves reduces but the individual volumes increase.

6. Results

First the results for the extreme individual overtopping events characterized by the 2% exceedance water layer thickness ($h_{2\%}$), 2% exceedance front velocity ($u_{2\%}$) and 2% exceedance individual overtopping volumes ($V_{2\%}$) in terms of incident waves are analysed in Section 6.1. Also, the distribution of the individual overtopping distribution in terms of overtopping events is analysed in Section 6.2 as this is important for probabilistic calculations. The individual overtopping volumes are obtained based on the water layer signal with the approach described in Sub Section 4.3.4.

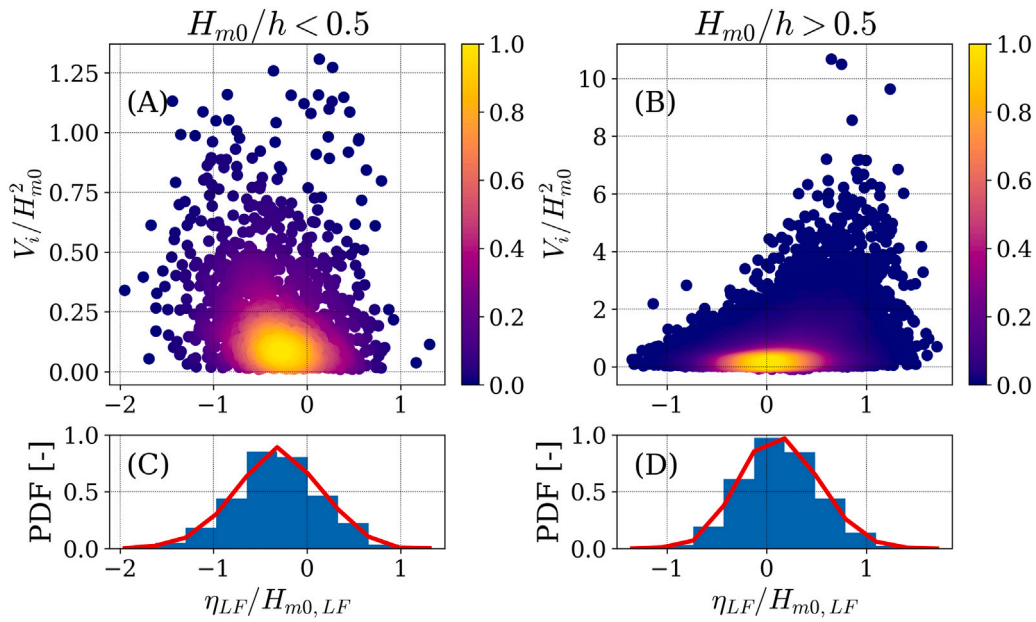


Fig. 5. Scatter density plot of the non-dimensional individual overtopping volume as a function of the water surface elevation of the low-frequency wave normalized with the low-frequency wave height (upper panels). The colours of the points indicate the normalized density of the point cloud. The lower panels show the histogram and probability density function of the overtopping events as a function of the surface elevation of the low-frequency wave normalized with the low-frequency wave height. The left panels corresponds to $H_{m0}/h < 0.5$ and the right panels to $H_{m0}/h > 0.5$.

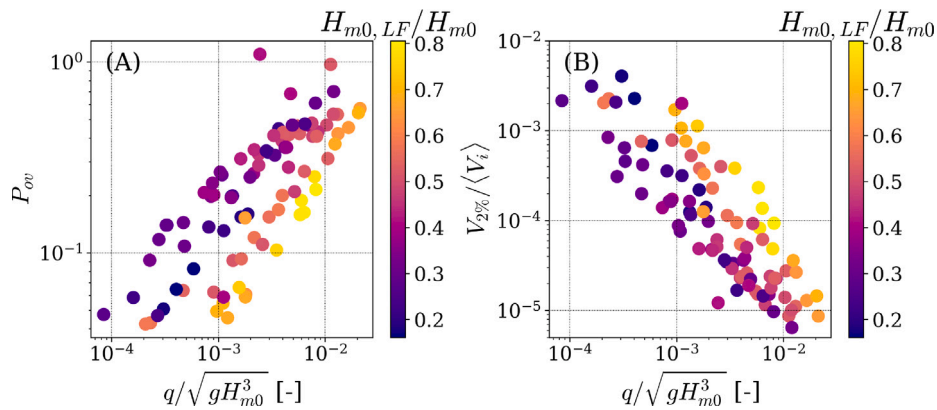


Fig. 6. Fraction of overtopping waves (P_{ov}) as a function of the non-dimensional overtopping discharge (Panel A) and the ratio between the 2% exceedance overtopping volume and the mean individual overtopping volume as a function of the non-dimensional overtopping volume (Panel B). The colours of the points indicate the relative low-frequency wave height.

6.1. Extreme individual overtopping events

6.1.1. Assessment of existing formulations

Table 4 presents the assessment of some formulations in literature for $h_{2\%}$, $u_{2\%}$ and $V_{2\%}$ at the middle of the crest for shallow water. For the $h_{2\%}$, Eqs. (1) and (3) with coefficients proposed by Van Gent (2002) (with $\gamma_f = 0.55$, $c_h = 0.15$ and $c_{c,h} = 0.4$) based on tests with dikes, Mares-Nasarre et al. (2019) (with $\gamma_f = 0.40$, $c_h = 0.52$ and $c_{c,h} = 0.89$) based on tests with a rubble mound breakwater and Koosheh et al. (2021) based on tests with a revetment (with $\gamma_f = 0.40$, $c_h = 0.24$ and $c_{c,h} = 0.40$) are verified. The roughness factor and runup formulation are applied as recommended of those studies. The $u_{2\%}$ is computed with Eqs. (2) and (4) with the coefficients proposed by Van Gent (2002) and with $u_{2\%} = 0.47\sqrt{gh_{2\%,B}/2}$ as proposed by Mares-Nasarre et al. (2019). Only the expression by Van Gent (2002) (Eq. (5)) is verified for $V_{2\%}$. To understand the impact of the choices in the various expressions, the results are also presented for the expression with fitted coefficients

based on this dataset showing that the existing formulations for $h_{2\%}$ are similar in accuracy but the choice of the expression has a more significant impact on $u_{2\%}$.

These results also show that the existing formulations perform reasonable to poor for rubble mound breakwaters in shallow water with a RMSE larger than 0.077 and 0.45 ($R^2 < 0$) for respectively the $h_{2\%}/H_{m0}$ and $u_{2\%}/\sqrt{gH_{m0}}$. The RMSLE found for the $V_{2\%}/H_{m0}^2$ is 2.26. These errors result in estimates that are off by significantly more than a factor of 20% for most conditions, where $u_{2\%}/\sqrt{gH_{m0}}$ is most accurately captured. The differences in the geometry (e.g. crest element or porous core) could explain the deviations with existing formulations. Another potential cause of the deviations could be the applied roughness factor which may not be valid for this model setup. Since fitting the coefficients in the expressions did not result in significant improvements, new expressions are required for a rubble mound breakwater in shallow water.

Table 4

Root mean square error (RMSE), Root mean square logarithmic error (RMSLE) and R^2 for various formulations existing in literature which describe the 2% exceedance water layer thickness, front velocity and volumes at the middle of the crest. The RMSE is shown for $h_{2\%}/H_{m0}$ and $u_{2\%}/\sqrt{gH_{m0}}$ and the RMSLE for $V_{2\%}/H_{m0}^2$.

| Variables | Expression | | RMSE or RMSLE [-] | R^2 |
|--------------------------|-------------------------------|----------|-------------------|-------|
| $h_{2\%}/H_{m0}$ | Van Gent (2002): | Proposed | 0.077 | <0 |
| | | Fitted | 0.05 | 0.50 |
| | Mares-Nassarre et al. (2019): | Proposed | 0.33 | <0 |
| | | Fitted | 0.05 | 0.44 |
| | Koosheh et al. (2021): | Proposed | 0.55 | <0 |
| | | Fitted | 0.05 | 0.44 |
| $u_{2\%}/\sqrt{gH_{m0}}$ | Van Gent (2002): | Proposed | 0.45 | <0 |
| | | Fitted | 0.41 | 0.02 |
| | Mares-Nassarre et al. (2020): | Proposed | 1.3 | <0 |
| | | Fitted | 0.70 | <0 |
| $V_{2\%}/H_{m0}^2$ | Van Gent (2002) (Eq. (5)): | Proposed | 1.40 | <0 |
| | | Fitted | 0.69 | 0.52 |

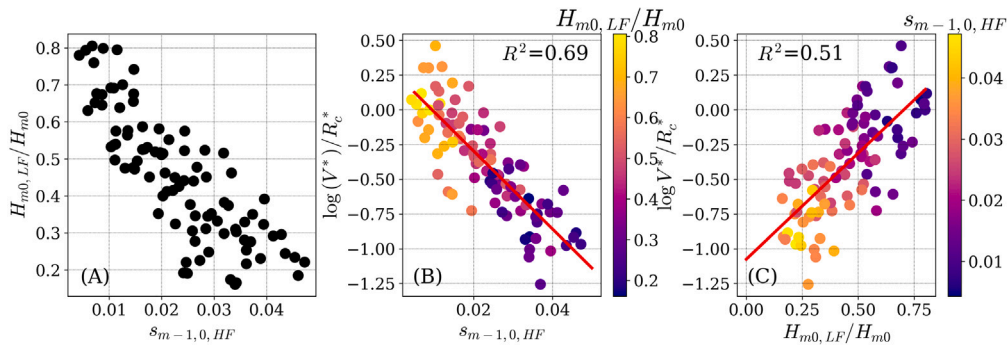


Fig. 7. Panel A shows the correlation between the relative low-frequency wave height ($H_{m0,LF}/H_{m0}$) and short-wave steepness ($s_{m-1,0,HF}$). Panel B shows $\log V^*/R_c^*$ as a function of the short-wave steepness where the colours represent the $H_{m0,LF}/H_{m0}$. Panel C shows $\log V^*/R_c^*$ as a function of the relative low-frequency wave height where the colours represent the $s_{m-1,0}$. The red line represents a linear fit.

6.1.2. Deriving formulations

To derive a new expression the same approach is applied for $h_{2\%}$, $u_{2\%}$ and $V_{2\%}$ which consists of the following steps:

1. Determine the most relevant non-dimensional variables based on a random forest regressor (see Appendix G).
2. Fit several functions and add variables one by one, to show the effect of a variable on the accuracy of the fit.
3. Apply the bootstrapping technique to determine robust coefficients with the 95% percentiles for the final proposed expression.

The variable sensitivity with the random forest regressor shows that the short-wave steepness and relative crest height are the most important variables followed by the low-frequency wave height (see Appendix G). Note that these parameters were found to be the most important for wave overtopping discharges as well (De Ridder et al., 2024). To explain why the low-frequency wave height does not appear as one of the most relevant variables, the high correlation between the $H_{m0,LF}/H_{m0}$ and $s_{m-1,0,HF}$ is shown in Panel A of Fig. 7; the effect of the $H_{m0,LF}/H_{m0}$ is indirectly captured by $s_{m-1,0,HF}$. Only considering the $H_{m0,LF}/H_{m0}$ seems not sufficient to capture, for example, the 2% exceedance volumes. When a logarithmic function is assumed for the relation between the relative crest height (R_c^*) and the non-dimensional overtopping volume as $V^* = a \exp(-bR_c^*)$, it is possible to derive a non-dimensional overtopping volume including the effects of the crest height ($\log(V^*)/R_c^*$). This non-dimensional overtopping volume is plotted against the short-wave steepness and the low-frequency wave height in Panels B and C of Fig. 7. This result shows that most of the remaining scatter is explained by the short-wave steepness (Panel B, $R^2 = 0.69$) compared to $H_{m0,LF}/H_{m0}$ (Panel C, $R^2 = 0.51$). Thus, it is better to describe the effect of the low-frequency wave height with the short-wave steepness in shallow water.

The common functions to describe the 2% exceedance water layer thickness, front velocity or individual overtopping volumes in literature are based on the difference between the 2% exceedance runup and the crest height (See Eqs. (1), (2) and (5)). It is chosen not to follow this approach here because it is not trivial to distinguish between the short and long waves with the existing expressions for the runup height and no 2% runup measurements are available in this study. Instead, an exponential formulation based on the relative crest height, similar to the typical overtopping formulation, is used to estimate the 2% exceedance water layer thickness and individual overtopping volumes, as both show a high correlation with the non-dimensional mean overtopping discharge (not shown). Furthermore, an advantage of the exponential function is that the desired physical behaviour is included in the formulation with $h_{2\%} \rightarrow 0$ for $R_c/H_{m0} \rightarrow \infty$. For the front velocity, a power function is applied because it is reasoned that the effect of the crest height is less pronounced. The other variables are included as a factor for the relative crest or included in the relative crest.

Based on the previous findings the following formulations are proposed and assessed for each extreme individual overtopping variables,

- Function of the relative crest (R_c/H_{m0})
- Function of the relative crest (R_c/H_{m0}) and wave steepness ($s_{m-1,0}$)
- Function of the relative crest (R_c/H_{m0}) and short-wave steepness ($s_{m-1,0,HF}$)
- Function of the relative crest corrected for the low-frequency wave height ($(R_c - cH_{m0,LF})/H_{m0}$) and short-wave steepness ($s_{m-1,0,HF}$)
- Function of the relative crest based on the 2% exceedance wave height ($R_c/H_{2\%}$) and short-wave steepness ($s_{m-1,0,HF}$)

- Function of the relative crest based on the 2% exceedance wave height and corrected for the low-frequency wave height ($(R_c - cH_{m0,LF})/H_{2\%}$) and short-wave steepness ($s_{m-1,0,HF}$)

In these formulations, the effect of the wave steepness is included in both the wave steepness and the short-wave steepness. The contribution of the low-frequency wave height next to the influence of the short-wave steepness is verified by accounting for the water level variation in the relative crest height (as proposed by Van Gent, 2021, 2023; De Ridder et al., 2023). The effect of wave breaking and a non-Rayleigh distributed wave field is incorporated in the 2% exceedance wave height. All the formulations are fitted with a roughness factor (γ_f) which is set to 0.55 (rocks two layers according to TAW, 2002).

The expressions are fitted with a nonlinear optimization method which minimizes the sum of the squares of the differences between the observations and the predictions. To obtain a robust estimate of the coefficients a bootstrapping technique is applied. Every fit is performed 150 times with a sampled dataset of size N from the total dataset of size N . Thus, the same data entries can be present multiple times in the sampled dataset or not be present at all. The mean coefficient is applied as the estimate of the coefficient. The 95% percentiles of the coefficients are computed for the proposed expression based on the obtained distribution of the parameter (see Appendix F for the results). The 90% confidence interval is computed based on the methodology in Herrera and Medina (2015) with the assumption of a Gaussian distribution of the error with a mean error of 0. For example, for variable X , the confidence interval is given by,

$$X|_{5\%}^{95\%} = X \pm 1.64\sqrt{aX + b} \quad (22)$$

where the variance, $\sigma^2 = aX + b$, is based on a binned linear fit of σ^2 with respect to X . For the volumes the linear fit is based on the logarithmic error.

6.1.3. Water layer thickness

It is found that the short-wave steepness ($s_{m-1,0,HF}$) is the most relevant wave variable to describe the water layer thickness for this dataset (see Fig. 8). A low wave steepness condition results in a larger $h_{2\%}$ up to 40% of the wave height. This is much lower for short waves ($s_{m-1,0,HF} > 0.03$) where the $h_{2\%}$ is a maximum of 15% of the H_{m0} independently of the variations in the relative crest height. This difference can be explained by the fact that fewer waves break in the low wave steepness conditions resulting in larger $h_{2\%}$ at the crest. Besides the $s_{m-1,0,HF}$, the R_c/H_{m0} also influences the $h_{2\%}$. As expected, a lower relative crest height results in a larger water layer thickness compared to a higher relative crest height.

To quantify the effect of the wave variables on the water layer thickness, various functions are fitted adding explanatory variables one by one. In Table 5 the formulations are shown with the corresponding error. When only the dimensional crest height is included in the formulation to estimate $h_{2\%}/H_{m0}$ a $R_{adj}^2 = 0.20$ (RMSE of 0.062) is found for the $h_{2\%}/H_{m0}$. The fit significantly improves when the wave steepness is included in the expression with a R_{adj}^2 increase from 0.20 to 0.75. Also, the power of the steepness becomes larger showing that the contribution of $s_{m-1,0,HF}$ is more significant than $s_{m-1,0}$. A second improvement is found when the short-wave steepness is applied (R_{adj}^2 from 0.75 to 0.84). The influence of $H_{m0,LF}$ and $s_{m-1,0,HF}$ is also verified without a significantly improvement (Eq. (26)). Only the combination of $H_{m0,LF}$ and $H_{2\%}$ results in a small improvement (Eq. (28)). However, this improvement is so limited that Eq. (25) from Table 5 is preferred (see Fig. 9). The 95% percentiles of the coefficients in Eq. (25) are shown in Appendix F.

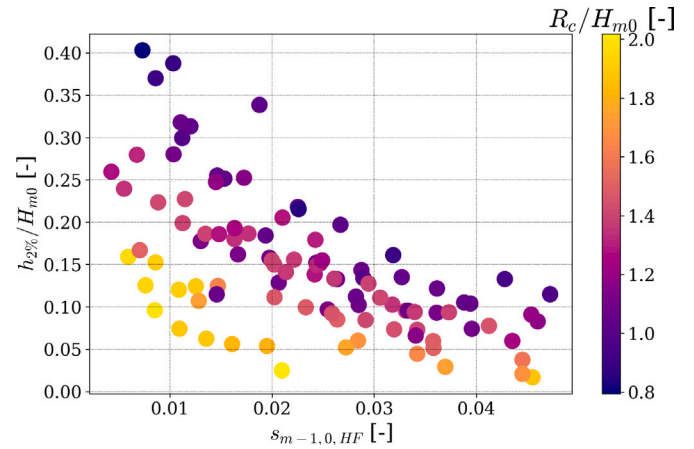


Fig. 8. 2% exceedance water layer thickness ($h_{2\%}$) normalized by the wave height (H_{m0}) as function of the short-wave steepness ($s_{m-1,0,HF}$). The colours of the points show the relative crest height expressed in the crest height divided by the wave height.

Table 5

Root mean square error (RMSE) and adjusted coefficient of determination (R_{adj}^2) for various formulations which describe the 2% exceedance water layer thickness. The roughness factor (γ_f) is set to 0.55.

| Function | | $h_{2\%}/H_{m0}$ [-] | RMSE | R_{adj}^2 |
|--|------|----------------------|-------|-------------|
| $h_{2\%}/H_{m0} = 0.53 \exp\left(-0.58 \frac{R_c}{H_{m0}\gamma_f}\right)$ | (23) | | 0.062 | 0.20 |
| $h_{2\%}/H_{m0} = 0.82 \exp\left(-2.28 \frac{R_c}{H_{m0}\gamma_f} s_{m-1,0}^{0.21}\right)$ | (24) | | 0.035 | 0.75 |
| $h_{2\%}/H_{m0} = 0.63 \exp\left(-4.88 \frac{R_c}{H_{m0}\gamma_f} s_{m-1,0,HF}^{0.50}\right)$ | (25) | | 0.028 | 0.84 |
| $h_{2\%}/H_{m0} = 0.53 \exp\left(-4.80 \frac{R_c - 0.35H_{m0,LF}}{H_{m0}\gamma_f} s_{m-1,0,HF}^{0.50}\right)$ | (26) | | 0.027 | 0.84 |
| $h_{2\%}/H_{m0} = 0.63 \exp\left(-6.93 \frac{R_c}{H_{2\%}\gamma_f} s_{m-1,0,HF}^{0.53}\right)$ | (27) | | 0.029 | 0.82 |
| $h_{2\%}/H_{m0} = 0.47 \exp\left(-6.07 \frac{R_c - 0.69H_{m0,LF}}{H_{2\%}\gamma_f} s_{m-1,0,HF}^{0.48}\right)$ | (28) | | 0.026 | 0.86 |

^a Eq. (25) is recommended.

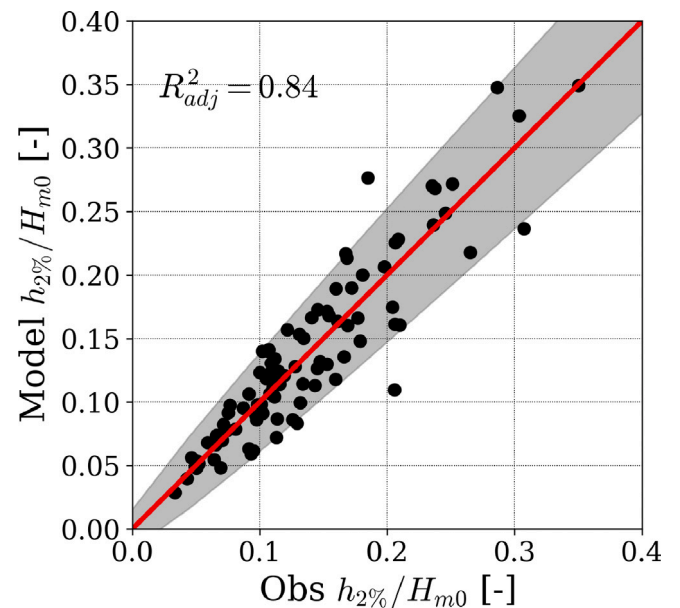


Fig. 9. Comparison of measured (Obs) and estimated (Model) $h_{2\%}/H_{m0}$ using Eq. (25). The gray band show the 90% confidence using a and b for Eq. (22) given by 0.0057 and 0 respectively.

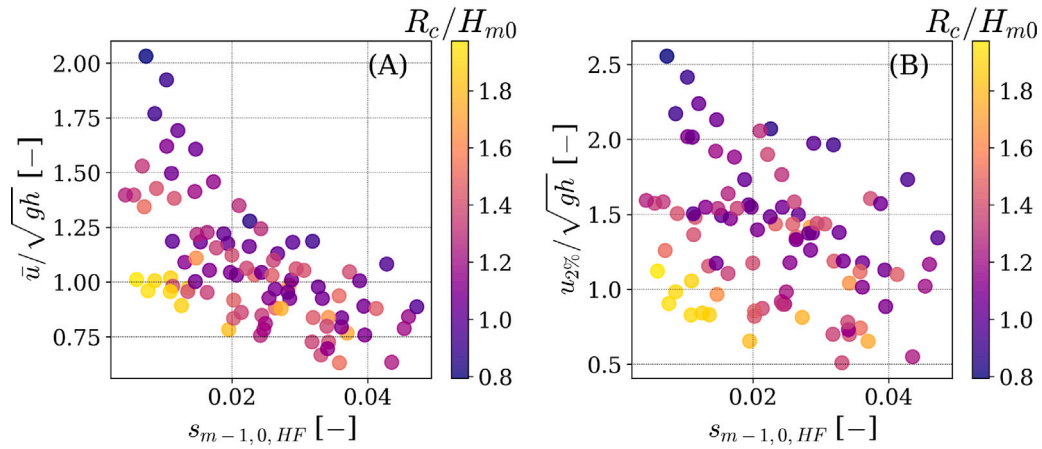


Fig. 10. Short-wave steepness as a function of the front velocity divided by the shallow water wave celerity for the mean front velocity (Panel A) and the 2% exceedance front velocity (Panel B). The colours represent the relative crest height.

6.1.4. Front velocity

Two front velocities were analysed. The mean front velocity over the test (\bar{u}) and the 2% exceedance velocity in terms of incident waves ($u_{2\%}$). The \bar{u} contains less uncertainty and thus it is used to obtain insights into the influence of variables. Various normalization variables were verified but the best results were observed for a normalization with the shallow water wave celerity (\sqrt{gh}) which also has a physical justification.

The results of \bar{u} (Panel A) and $u_{2\%}$ (Panel B) are shown in Fig. 10 with the colours representing the relative crest height. The \bar{u}/\sqrt{gh} becomes larger for a smaller $s_{m-1,0,HF}$ with \bar{u} equal to 2 times \sqrt{gh} . For these conditions, the actual wave celerity is most likely to be larger than \sqrt{gh} because of the large amounts of low-frequency waves which temporally increase the water depth resulting in a larger wave celerity than obtained with the still water depth (h). In addition, the distance between the crest and the still waterline becomes smaller for conditions with a temporal increase in the water depth (due to low-frequency waves). For the high $s_{m-1,0,HF}$ conditions, \bar{u}/\sqrt{gh} is lower than \sqrt{gh} . The effects of the crest level are also visible with larger crest levels resulting in lower \bar{u}/\sqrt{gh} . Similar behaviour is visible for $u_{2\%}/\sqrt{gh}$ but the effect of the relative crest level seems more pronounced, especially for the low $s_{m-1,0,HF}$ where $u_{2\%}$ varies between 0.5 and 2.2 times \sqrt{gh} .

The results for the expressions of the non-dimensional $u_{2\%}$ are shown in Table 6. Although the scatter are still relatively large (R_{adj}^2 of 0.55 for Eq. (31)), similar results to the $h_{2\%}/H_{m0}$ are observed. The most important wave variables to predict the front velocities are the relative crest height and $s_{m-1,0,HF}$, which result in an $R_{adj}^2 = 0.55$ (RMSE of 0.29). The best match was found for Eqs. (31), (33), and (34) although the improvement of Eqs. (33) and (34) compared to Eq. (31) is limited. The similar results of the non-dimensional mean front velocity (shown in Table E.11) with less scatter ($R_{adj}^2 = 0.69$, see also Panel B of Fig. 11) suggest that the relevant variables are included in the expression. Moreover, the scatter of these expressions is significantly lower than observed for the existing formulations (see Table 4), and also for different normalizations. A comparison between measured and estimated velocities using Eqs. (31) and Eq. (E.3) for respectively $u_{2\%}/\sqrt{gh}$ and \bar{u}/\sqrt{gh} are shown in Fig. 11.

6.1.5. 2% exceedance overtopping volume

In Fig. 12, the 2% exceedance non-dimensional overtopping volumes are shown as a function of the relative crest height and the short-wave steepness. As expected, the 2% exceedance non-dimensional overtopping volume increases when the relative crest height becomes lower. The short-wave steepness also has a large effect; wave conditions with a larger wave steepness result in significantly lower $V_{2\%}/H_{m0}^2$ compared to a test with the same relative crest height.

Table 6

RMSE and adjusted coefficient of determination for the expression for the 2% exceedance front velocity at the middle of the crest for various functions. The roughness factor (γ_f) is set to 0.55.

| Function | $u_{2\%}/\sqrt{gh}$ [-] | RMSE | R_{adj}^2 |
|--|-------------------------|------|-------------|
| | | | |
| $u_{2\%}/\sqrt{gh} = 3.14 \left(\frac{R_c}{H_{m0}\gamma_f} \right)^{-1.04}$ (29) | | 0.35 | 0.37 |
| $u_{2\%}/\sqrt{gh} = 1.96 \left(\frac{R_c}{H_{m0}\gamma_f} \right)^{-1.13} s_{m-1,0}^{-0.11}$ (30) | | 0.31 | 0.51 |
| $u_{2\%}/\sqrt{gh} = 1.26 \left(\frac{R_c}{H_{m0}\gamma_f} \right)^{-1.05} s_{m-1,0,HF}^{-0.24}$ (31) | | 0.29 | 0.55 |
| $u_{2\%}/\sqrt{gh} = 1.29 \left(\frac{R_c - 0.07 H_{m0,LF}}{H_{m0}\gamma_f} \right)^{-1.02} s_{m-1,0,HF}^{-0.22}$ (32) | | 0.29 | 0.51 |
| $u_{2\%}/\sqrt{gh} = 0.85 \left(\frac{R_c}{H_{2\%}\gamma_f} \right)^{-1.02} s_{m-1,0,HF}^{-0.27}$ (33) | | 0.30 | 0.55 |
| $u_{2\%}/\sqrt{gh} = 1.05 \left(\frac{R_c - 0.47 H_{m0,LF}}{H_{2\%}\gamma_f} \right)^{-0.85} s_{m-1,0,HF}^{-0.15}$ (34) | | 0.29 | 0.54 |

^a Eq. (31) is recommended.

The $s_{m-1,0,HF}$ is also here an important variable. The R_{adj}^2 increases from 0.16 to 0.77 when the steepness is included in the expression. A further improvement is visible when $s_{m-1,0}$ is replaced by $s_{m-1,0,HF}$ (RMSLE of 0.34 and $R_{adj}^2 = 0.85$). The addition of $H_{2\%}$ in the relative crest does not improve the fit (Eq. (39)). The addition of the low-frequency wave height in the relative crest height only improves the accuracy in combination with the 2% exceedance volumes but the effect is limited ($R_{adj}^2 = 0.87$). Thus, Eq. (37) is proposed as final formulation (see Fig. 13).

6.2. Individual overtopping volume distribution

The error of the fitted distribution is lower when the log-normal distribution is applied instead of the 2-parameter Weibull distribution (see Table 8) as found in Mares-Nasarre et al. (2024). Here instead of fitting both the shape and scale parameters, the shape parameter is based on the mean shape factor over all tests. For each test where the number of individual overtopping events is larger than 75 and the non-dimensional overtopping discharge is larger than 10^{-5} , a log-normal distribution (Eq. (7)) is fitted with a constant shape (shape factor of 0.90). To derive a formulation for the scale parameter, k_v , (see Appendix C for the definition), the obtained k_v are related to the wave variables. Since the unit of k_v is equal to the overtopping volume, k_v is normalized with H_{m0}^2 .

Note that the fitted distribution is in terms of individual overtopping volumes and is not expressed in terms of the number of incident waves.

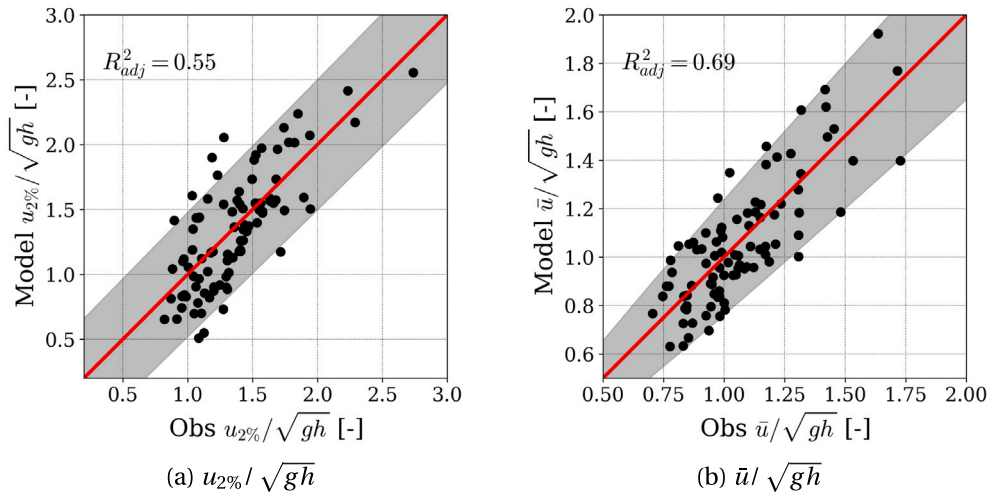


Fig. 11. Comparison of measured (Obs) and estimated (Model) $u_{2\%}/\sqrt{gh}$ using Eq. (31) and \bar{u}/\sqrt{gh} using Eq. (E.3). The gray band show the 90% confidence computed with Eq. (22) using $a = 0.024$ and $b = -0.003$ for \bar{u}/\sqrt{gh} and $a = 0.0081$ and $b = 0.076$ for $u_{2\%}/\sqrt{gh}$.

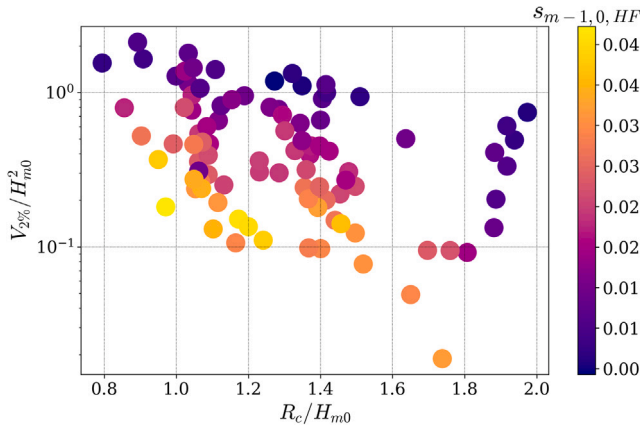


Fig. 12. Non-dimensional 2% exceedance overtopping volumes in terms of number of waves as a function of the relative crest height. The colours indicate the short-wave steepness. Results are obtained for tests with at least 50 overtopping events and a non-dimensional mean overtopping discharge larger than 10^{-5} .

Table 7

RMSLE and adjusted coefficient of determination for the expression to describe the 2% exceedance overtopping volumes in terms of incident waves. A roughness factor (γ_f) of 0.55 is applied.

| Function | | $V_{2\%}/H_{m0}^2$ [-] | RMSLE | R^2_{adj} |
|--|------|------------------------|-------|-------------|
| $V_{2\%}/H_{m0}^2 = 2.43 \exp\left(-0.76 \frac{R_c}{H_{m0}\gamma_f}\right)$ | (35) | | 0.82 | 0.16 |
| $V_{2\%}/H_{m0}^2 = 6.61 \exp\left(-3.72 \frac{R_c}{H_{m0}\gamma_f} s_{m-1,0}^{0.23}\right)$ | (36) | | 0.43 | 0.77 |
| ^a $V_{2\%}/H_{m0}^2 = 5.56 \exp\left(-9.94 \frac{R_c}{H_{m0}\gamma_f} s_{m-1,0,HF}^{0.57}\right)$ | (37) | | 0.34 | 0.85 |
| $V_{2\%}/H_{m0}^2 = 4.14 \exp\left(-9.62 \frac{R_c - 0.36 H_{m0,LF}}{H_{m0}\gamma_f} s_{m-1,0,HF}^{0.56}\right)$ | (38) | | 0.33 | 0.86 |
| $V_{2\%}/H_{m0}^2 = 5.03 \exp\left(-13.64 \frac{R_c}{H_{2\%}\gamma_f} s_{m-1,0,HF}^{0.60}\right)$ | (39) | | 0.36 | 0.84 |
| $V_{2\%}/H_{m0}^2 = 3.10 \exp\left(-11.29 \frac{R_c - 0.77 H_{m0,LF}}{H_{2\%}\gamma_f} s_{m-1,0,HF}^{0.52}\right)$ | (40) | | 0.31 | 0.87 |

^a Eq. (37) is recommended.

To obtain the probabilities in terms of incident waves, Eq. (10) can be used. Also, note that by fitting k_v and setting the shape parameter to a constant value, the mean of the fitted distribution does not correspond

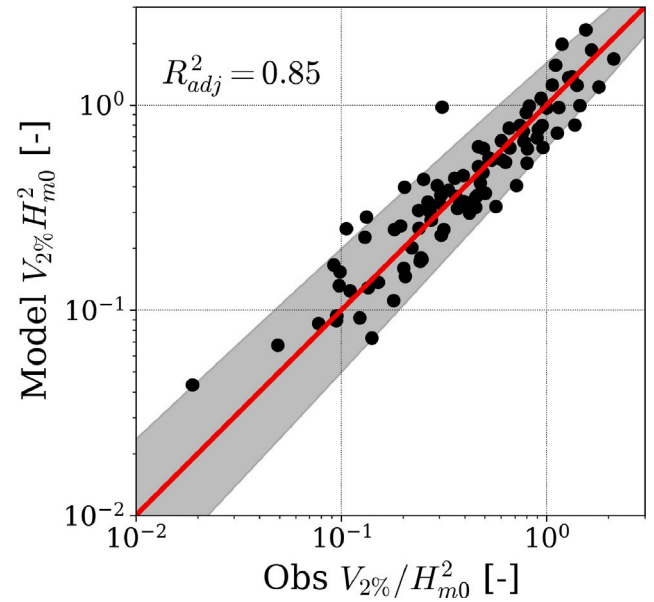


Fig. 13. Comparison of measured (Obs) and estimated (Model) $V_{2\%}/H_{m0}^2$ using Eq. (37). The gray band show the 90% confidence computed with Eq. (22) using $a = -0.04$ and $b = -0.086$.

to the mean individual volume (\bar{V}). However, it is argued that for design purposes it is more important to capture the distribution of the volumes accurately than to obtain a distribution with a very accurate mean. Furthermore, a second formulation would be needed to describe the mean individual overtopping volumes if the mean volume would be included in the distribution. In practical applications, this would reduce the accuracy because two formulations each with their uncertainty would be required to describe the individual overtopping distribution (accumulating errors).

In Table 9, the results for various formulations are shown. The error reduces when the wave steepness is included in the formulation next to the relative crest height. A second improvement is obtained when the short-wave steepness is applied (RMSLE = 0.32 and $R^2_{adj} = 0.78$). The results of including the low-frequency wave height and the 2% exceedance wave height did not improve the formulations and are therefore not shown in Table 9. Thus, Eq. (43) is the preferred formulation describing k_v of the log-normal distribution (see Panel C of Fig. 14).

Table 8

RMSLE for fitted distributions when different expressions are applied to describe the distribution.

| Function | V_i/H_{m0}^2 [-] | |
|---|--------------------|-------|
| | RMSLE | R^2 |
| Weibull with fitted scale parameter | 0.41 | 0.85 |
| Log-normal with fitted scale parameter (Eq. (43)) | 0.34 | 0.90 |
| Weibull - $b = 0.75$ (using measured q) | 1.03 | 0.10 |
| Mares-Nasarre et al. (2024) | 0.65 | 0.64 |

Table 9

RMSLE and adjusted coefficient of determination for the expression to describe the scale parameter of the log-normal distribution.

| Function | | k_V/H_{m0}^2 [-] | |
|---|------|--------------------|-------------|
| | | RMSLE | R_{adj}^2 |
| $k_V/H_{m0}^2 = 0.14 \exp\left(-0.06 \frac{R_c}{H_{m0}}\right)$ | (41) | 0.70 | -0.01 |
| $k_V/H_{m0}^2 = 0.49 \exp\left(-9.04 \frac{R_c}{H_{m0}} s_{m-1,0}^{0.45}\right)$ | (42) | 0.36 | 0.73 |
| $^a k_V/H_{m0}^2 = 0.48 \exp\left(-38.26 \frac{R_c}{H_{m0}} s_{m-1,0,HF}^{0.95}\right)$ | (43) | 0.32 | 0.78 |

^a Eq. (43) is recommended.

The volume distributions obtained with Eq. (43) for the scale parameter are shown in Fig. 14 (Panel A). The obtained accuracy of the fitted distribution is given by $R_{adj}^2 = 0.90$ (RMSLE = 0.34, see Table 8). To evaluate the accuracy of the tail of the fitted distribution using Eq. (43) for the scale parameter, the 2% exceedance volume is compared to the measured 2% exceedance volume. Note that this exceedance volume ($V_{2\%,ov}$) is expressed in terms of the overtopping events and not in terms of incident waves as shown in Table 7. The found RMSLE for the non-dimensional 2% exceedance overtopping volume is 0.38.

When the Weibull distribution (Eq. (6)) with a shape parameter of 0.75 and a scale parameter defined by $\frac{1}{\Gamma(1+1/0.75)} \bar{V}$ is applied, the RMSLE is 0.51. However, in this approach, the mean individual volume (\bar{V}) is based on the measured mean overtopping discharge instead of the estimated mean overtopping discharge making the fit significantly better than when the estimate of the mean overtopping discharge is applied. Thus, in practical applications, the error will be larger because the mean individual volume has to be determined with another formulation. When the approach described in the EurOtop (2018) is applied with the formulations for \bar{V} , the error is significantly higher (RMSLE = 4.3, not shown in Fig. 14). The Weibull distribution function depends on q , P_{ov} and the scale parameter b . Both b and P_{ov} depend on the mean overtopping discharge (q) making this approach very sensitive to accumulated errors. The proposed expression describing the scale parameter (Eq. (43)) does not depend on other empirical formulations making it significantly more accurate. Also the expressions (Eqs. (8) and (9)) for the shape and scale parameter of the log-normal distribution (see Appendix C for the definition used in Mares-Nasarre et al., 2024) as derived in Mares-Nasarre et al. (2024) are compared with the current datasets. This expression also shows reasonable results with an RMSLE of 0.69, but it requires more wave variables than Eq. (43).

The reasonable results for the formulation of the individual overtopping distribution with a constant shape factor show that the shape of the distribution does not change significantly for the different wave conditions.

6.2.1. Fraction of overtopping waves

When the volume distribution is given in terms of overtopping events, the fraction of overtopping events is required to transform the probabilities to exceedance probabilities in terms of incident waves. The existing formulations for the P_{ov} are evaluated with the current dataset in Table 10. The best results with existing expressions are obtained with the formulation of Mares-Nasarre et al. (2020), which was derived for depth-limited wave conditions with an R^2 of 0.47.

Table 10

RMSLE and adjusted coefficient of determination for various formulations describing the fraction of overtopping waves (P_{ov}). The upper four rows show the results for existing formulations (R^2).

| Function | | P_{ov} [-] | |
|---|------|--------------|----------------------|
| | | RMSLE | R_{adj}^2 or R^2 |
| Besley (1998): Eq. (11) | | 0.68 | 0.36 |
| EurOtop (2018): Eq. (12) | | 1.72 | <0 |
| Molines et al. (2019): Eq. (14) | | 1.20 | <0 |
| Mares-Nasarre et al. (2020): Eq. (15) | | 0.61 | 0.47 |
| $P_{ov} = 4.22 \exp\left(-2.34 \frac{R_c}{H_{m0}}\right)$ | (44) | 0.49 | 0.63 |
| $^a P_{ov} = 4.85 \exp\left(-3.14 \frac{R_c}{H_{m0}} s_{m-1,0,HF}^{0.06}\right)$ | (45) | 0.48 | 0.64 |
| $P_{ov} = 4.42 \left(\frac{q}{\sqrt{9.81 H_{m0}^3}}\right)^{0.51}$ | (46) | 0.52 | 0.59 |
| $P_{ov} = 208 \left(\frac{q}{\sqrt{9.81 H_{m0}^3}}\right)^{0.66} s_{m-1,0,HF}^{0.74}$ | (47) | 0.37 | 0.78 |

^a Eq. (45) is recommended.

In Fig. 6, it is observed that the fraction of overtopping waves for the same non-dimensional overtopping discharge is related to the low-frequency wave height. To quantify this effect, several empirical formulations are fitted. Two approaches exist in literature to describe the fraction of overtopping waves. The ratio of overtopping waves as a function of the incident waves, P_{ov} , can be related to the mean overtopping discharge as given in Mares-Nasarre et al. (2020) or to the wave variables and relative crest height as proposed in EurOtop (2018). An expression including q for P_{ov} can be used to show the additional effects next to the q assuming that the mean overtopping discharge is the dominant variable for predicting the P_{ov} . However, for practical applications, such an approach requires an additional formulation to estimate q which leads to accumulated errors.

When using an expression based on the non-dimensional overtopping discharge, it was found relevant to include the $s_{m-1,0,HF}$. The R_{adj}^2 reduced from 0.59 (Eq. (46)) to 0.78 (Eq. (47)) when $s_{m-1,0,HF}$ is included. It is verified whether the low-frequency wave height ($H_{m0,LF}/H_{m0}$) instead of $s_{m-1,0,HF}$ would improve the error but this would lead to slightly higher R_{adj}^2 . Thus, next to $H_{m0,LF}/H_{m0}$ also $s_{m-1,0}$ affects P_{ov} in combination with the non-dimensional mean overtopping discharge. The accuracy is less influenced by the $s_{m-1,0,HF}$ when the relative crest height is applied instead of the non-dimensional overtopping discharge in the expression (Eqs. (44) and (45)). The formulation with the short-wave steepens results in the lowest error (Eq. (45), see also Fig. 15). Thus, Eq. (45) is recommended to estimate the fraction of overtopping waves. While it performs similarly to Mares-Nasarre et al. (2020), it has the advantage of not including the mean wave overtopping discharge in the expression.

7. Discussion

For all three extreme individual overtopping variables ($h_{2\%}$, $u_{2\%}$ and $V_{2\%}$), the error found for the newly fitted function is lower than the existing formulations (see Table 4). Still, scatter is present in the expressions which may be caused by several reasons. First, the absolute distance between the start of the crest and the location of the water layer thickness (halfway at the crest) is fixed (0.25 m), but this does not correspond to the same relative distance (e.g. $B/L_{m-1,0}$ or B/H_{m0}) taking into account the various model scales. Eqs. (3) and (4) do not include wave variables but likely, this distance is also related to a hydrodynamic length scale, such as the wavelength described in Bosman et al. (2009). However, it is verified whether the same formulations hold at another crest location using a different water layer thickness instrument. Since the formulations show similar results at this other location, it indicates that the potential scatter caused

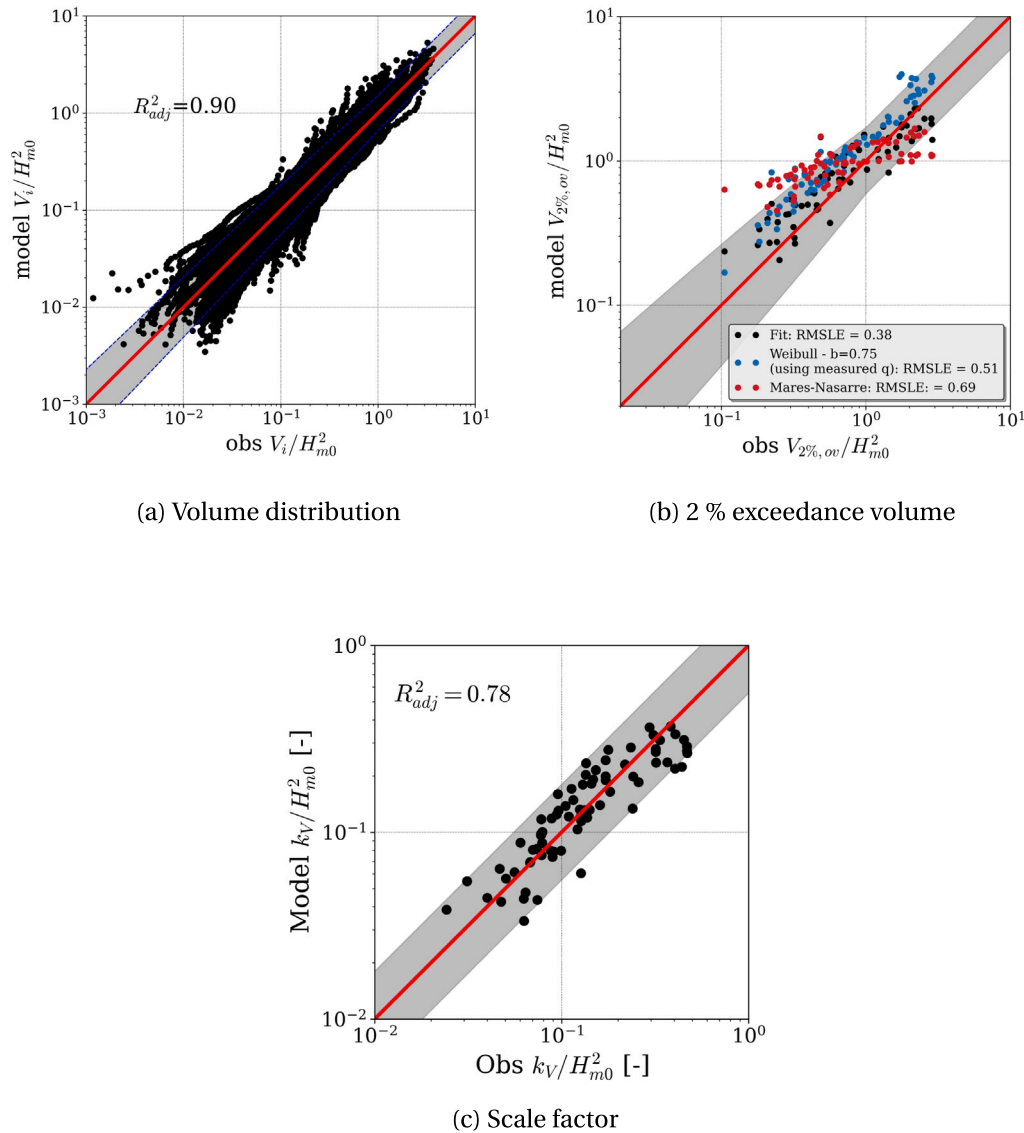


Fig. 14. Comparison of measured (Obs) and estimated (Model) volumes: (a) distribution of V_i/H_{m0}^2 , (b) $V_{2\%,ov}/H_{m0}^2$, and (c) scale factor (k_V/H_{m0}^2). The gray band show the 90% confidence computed with Eq. (22) using $a = -0.027$ and $b = 0.063$ for V_i/H_{m0}^2 , $a = -0.11$ and $b = 0.10$ for $V_{2\%,ov}/H_{m0}^2$ and $a = 0.013$ and $b = 0.13$ for k_V/H_{m0}^2 .

by the relative location is lower than the included wave variables in the expression. It is also verified whether the remaining scatter is related to the relative distance but no clear trend was observed. Another cause of the spreading could be the roughness. The same stones are applied for all tests, which means that the relative roughness is different between various tests (D_{n50}/H_{m0} varies between 0.12–0.67). It is verified whether the relative roughness in the fit would improve the accuracy, but no improvement was obtained for the current dataset. Lastly, the estimate of the $h_{2\%}$, $u_{2\%}$ and $V_{2\%}$ also contain scatter, which especially for very small water layer thickness can be significant.

The individual overtopping volumes are measured here indirectly based on the water layer thickness instruments. This study showed that only considering the overtopping box may not be sufficient. However, the individual overtopping volumes obtained from the water layer thickness instruments may contain a large measurement uncertainty as both the water layer thickness and velocity are required. The consistent trends for the individual overtopping volumes (and also water layer thickness and velocities) indicate that the individual overtopping volumes are properly estimated, but the scatter could be caused by these uncertainties. Moreover, the magnitude of the individual overtopping

volumes is partially validated with the results from the overtopping box. Therefore, it is recommended to verify this approach with, for example, numerical models where the individual overtopping volumes can be directly measured. Moreover, it is recommended to also verify the value of c_v to make Eq. (17) generally applicable.

The current findings are applicable to a permeable structure with a 1:2 slope, including a non-protruding crest element. It should be verified whether the same findings are also valid for different structure characteristics (e.g. variation in armour, slope and permeability). However, it can be argued that the shallow-water processes affecting wave overtopping are independent of most structural characteristics, suggesting that similar trends should be observed for variations in geometry.

One of the key parameters for the expressions is the short-wave steepness ($s_{m-1,0,HF}$). Typically the wave steepness ($s_{m-1,0}$) is used in coastal engineering projects. Since both parameters need to be determined from a wave spectrum, it is argued that also the short-wave steepness is reasonably easy to obtain. Instead of integrating over all the frequencies to compute the spectral moment (e.g. for the zero-moment: $m_0 = \int_{f=0}^{f=f_{nyq}} E(f)df$), one needs to integrate over a certain frequency

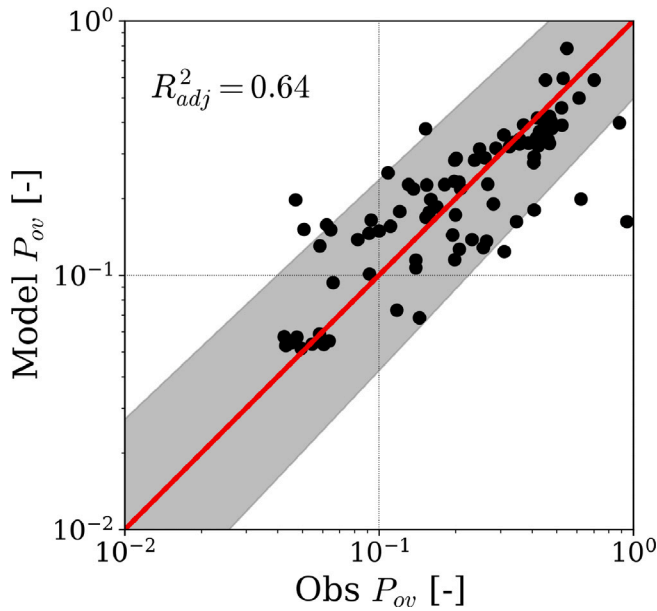


Fig. 15. Comparison of measured (Obs) and estimated (Model) P_{ov} using Eq. (45). The gray band show the 90% confidence computed with Eq. (22) using $a = -0.04$ and $b = 0.18$.

range (e.g. for the zero-moment: $m_0 = \int_{f=f_{cutoff}}^{f=f_{nyq}} E(f)df$ where $f_{cutoff} = 0.6/T_{m-1,0,deep}$).

Typically the extreme overtopping variables are computed with an expression related to $R_{u2\%}$. Using the proposed expression (e.g. Eq. (37)) and assuming the power of $s_{m-1,0,HF}$ is equal to 0.5, we find the following expression for the runup height $R_{u2\%}/H_{m0} = a \frac{1}{s_{m-1,0,HF}}$ with coefficient a . This expression is very similar to Eq. (A.1) when considering the definition of $\xi_{m-1,0}$ but applying $s_{m-1,0,HF}$ instead of $s_{m-1,0}$. Thus, it is recommended to validate the proposed formulation also based on experiments where the runup is measured.

Only the $V_{2\%}/H_{m0}^2$ is considered in this study but in literature also other exceedance values are considered (e.g. Koosheh et al., 2021). The reasonable fit with a constant shape factor for the individual overtopping distribution (see Table 8) shows that it is possible to relate the various exceedance values of the individual overtopping volumes. In Fig. 16, this is demonstrated by comparing various exceedance values ($V_{0.1\%}$, $V_{1\%}$, $V_{10\%}$ and $V_{20\%}$) with $V_{2\%}$. Especially, for the more extreme values this relation is relatively accurately predicted with a linear relation (e.g. R^2 of 0.88 for $V_{0.1\%}$). The error increases when the exceedance value is more extreme than $V_{2\%}$ as these values are less statistically stable. Conversely, values less extreme than $V_{2\%}$ also show larger errors likely due to the smaller volumes resulting in larger measurement errors.

Effects of the changing wave height distribution on the individual volume distribution could not be observed for individual overtopping volumes. Reasonable results were obtained with a constant shape factor for the volume overtopping distribution (see Fig. 14). Thus, the changing shape of the wave height distribution does not directly result in a different shape for the individual overtopping volumes. The effect of the low-frequency wave height on the individual overtopping volumes, water layer thickness and front velocities is shown (see Figs. D.20, D.21 and 5). No significant effect on the distribution of the events is observed (Panel D of Figs. D.20, D.21 and 5). However, the fraction of overtopping events as a result of the temporal water level variation changes significantly (see Fig. 6).

The findings in this study are valid for the ranges presented in Table 3, but it should be noted that the physical reasoning behind the expressions only applies to shallow water conditions where the

short waves cause overtopping and, thus, $s_{m-1,0,HF}$ is well defined. In conditions where only low-frequency waves are present a different approach is required, for example at a long fringing reef.

Capturing all these aspects in a physical formulation is challenging because of the correlations between the various variables. For example, the effect of the low-frequency wave energy is highly correlated to the short-wave steepness (as shown in Fig. 7) because longer waves result in significantly more energy transfer to lower frequencies. In addition, the low-frequency wave height is also present in the wave height, making it hard to distinguish the effects of low-frequency waves from the other aspects (wave steepness or crest height). The same holds for depth-induced wave breaking. Wave breaking can be captured with, for example the 2% exceedance wave height, but this variable is also affected by the low-frequency waves (shown in De Ridder et al., 2024). Thus, it is hard to derive an empirical formulation that includes all these processes separately.

8. Conclusions

In this study, extreme wave overtopping events at rubble mound structures with a smooth crest in shallow water are studied. The water layer thickness, front velocity and individual overtopping volumes are measured on the crest of rubble mound breakwaters. The experiments on a rubble mound breakwater with a rock armour layer on top of a permeable core, are performed for a large range of wave conditions ($0.80 < R_c/H_{m0} < 3.72$, $0.22 < h/H_{m0,deep} < 4.31$ and $0.004 < s_{m-1,0,HF} < 0.047$) and three different foreshores making the findings valid for wave conditions with severe wave breaking and large amounts of low-frequency waves where short-waves still cause overtopping.

The largest individual overtopping volumes arise from short waves which travel on the crest of a low-frequency wave in shallow water. In deep water, the opposite behaviour is observed where the largest waves and the resulting overtopping volumes are out of phase with the low-frequency wave. Due to the large amounts of energy at the lower frequencies in shallow water and the resulting temporal increase of the water level, the fraction of overtopping events is significantly lower but the overtopping events are larger compared to conditions without much energy at the lower frequencies.

Both the relative crest height and short-wave steepness significantly affect the $h_{2\%}$, $u_{2\%}$ and $V_{2\%}$. A new formulation (Eqs. (25), (31) and (37)) for shallow water is derived with a R^2 of 0.84 for the $h_{2\%}/H_{m0}$, R^2 of 0.55 for the $u_{2\%}/\sqrt{gh}$ and with a R^2 of 0.85 for the $V_{2\%}$. When also the 2% exceedance wave height and the low-frequency wave height are included, this error is further reduced to 0.86 for $h_{2\%}/H_{m0}$ and 0.87 for $V_{2\%}/H_{m0}^2$ (Eqs. (28) and (40)) but the improvement does not outweigh the needed additional parameters for the expression. This is a significant improvement to existing formulations with a RMSE of 0.07 for the $h_{2\%}/H_{m0}$ and 2.26 for the $V_{2\%}/H_{m0}^2$.

The log-normal distribution is recommended for the distribution of the individual overtopping volumes. By including the relative crest height and short-wave steepness in the expression for the scale parameter, the distribution can reasonably be predicted ($R^2 = 0.90$). Compared to most of the current design approaches which are based on a cascade of empirical formulations, this is a significant improvement. Furthermore, the reasonable results with a constant shape factor suggest that the shape of the distribution does not change significantly for shallow water conditions. Thus, the shallow foreshore mainly affects the fraction of overtopping events and the magnitude of these individual events. The fraction of overtopping events, needed to transform the distribution of overtopping volumes to a probability in terms of incident waves, seems related to the relative crest and the short wave steepness (Eq. (45)).

The results presented in this study confirm that the short-wave steepness and to a lower extent the low-frequency wave height are important variables in describing wave overtopping in shallow water, as found by De Ridder et al. (2024) for the mean overtopping discharge.

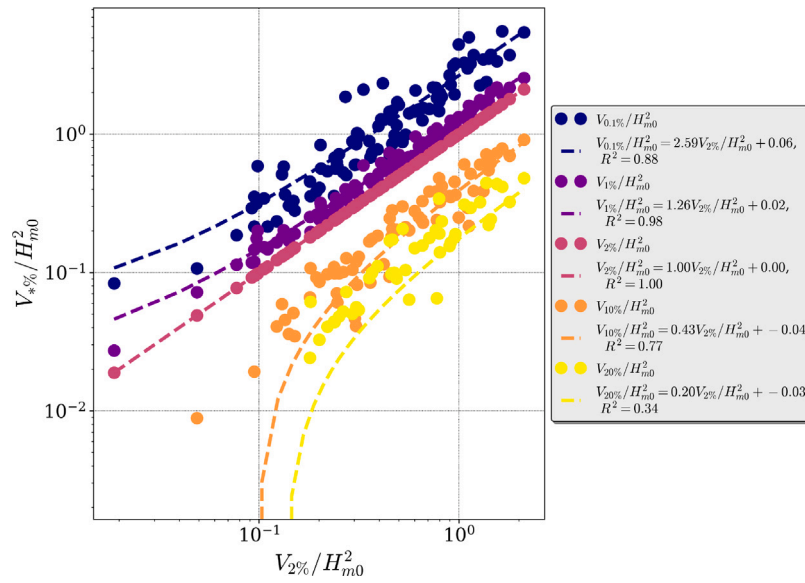


Fig. 16. Relation between $V_{2\%}/H_{m0}^2$ and other exceedance individual overtopping volumes ($V_{u\%}/H_{m0}^2$) expressed in terms of overtopping waves. For each exceedance individual volume, a linear fit is shown where the R^2 is computed based on $\log V_{u\%}/H_{m0}^2$.

CRedit authorship contribution statement

Menno P. de Ridder: Writing – original draft, Visualization, Methodology, Formal analysis. **Dennis C.P. van Kester:** Writing – review & editing, Funding acquisition. **Patricia Mares-Nassarre:** Writing – review & editing, Supervision, Investigation. **Marcel R.A. van Gent:** Writing – review & editing, Supervision, Investigation, Conceptualization.

Declaration of competing interest

The authors declare that they have no known competing financial interests or personal relationships that could have appeared to influence the work reported in this paper.

Acknowledgements

This study was conducted with the help of a TKI (Top Consortium for Knowledge and Innovation) subsidy (Delta Technology project CLIMACS, project DEL171) and support by the ‘Vereniging van Waterbouwers’. The assistance by our colleague Mr. Wesley Stet during the actual model testing is highly appreciated.

Appendix A. Runup formulations

The runup formulation of Van Gent (2001) is given by,

$$\frac{R_{u\%}}{H_{m0}\gamma_f} = \begin{cases} c_0\xi_{m-1,0} & \xi_{m-1,0} \leq p \\ c_1 - \frac{c_2}{\xi_{m-1,0}} & \xi_{m-1,0} > p \end{cases} \quad (\text{A.1})$$

where H_{m0} is the significant wave height, γ_f is a reduction factor, $\xi_{m-1,0}$ the Iribarren number. The coefficients c_2 and p are given by,

$$c_2 = 0.25 \frac{c_1^2}{c_0} \quad (\text{A.2})$$

$$p = 0.5 \frac{c_1}{c_0} \quad (\text{A.3})$$

The TAW (2002) formulation for the runup including only the influence factor for the roughness is given by,

$$\frac{R_{u\%}}{H_{m0}} = 1.65\gamma_f\xi_{m-1,0} \quad (\text{A.4})$$

with a maximum of

$$\frac{R_{u\%}}{H_{m0}} = \gamma_{surging} \left(4 - \frac{1.5}{\sqrt{\xi_{m-1,0}}} \right) \quad (\text{A.5})$$

where $\gamma_{surging}$ is related to Iribarren number and the roughness factor (γ_f),

$$\gamma_{surging} = \gamma_f + \frac{(\xi_{m-1,0} - 1.8)(1 - \gamma_f)}{8.2} \quad (\text{A.6})$$

Appendix B. Individual overtopping volumes

It is concluded for the performed tests, that the individual overtopping volumes cannot be accurately determined based on the signal from the overtopping box. When overtopping events occur quickly in succession, they become indistinguishable from the signal obtained from the overtopping box (see Fig. 4). Therefore, the individual overtopping volumes are determined based on Eq. (17). To validate this approach the total volume obtained from the overtopping box is compared to the total volume obtained with the approach based on Eq. (17).

This comparison is performed for all tests where the non-dimensional overtopping discharge is larger than 10^{-5} , without significant pumping time (less than 10%) and at least 50 overtopping events. When the cumulative overtopping volume signals are compared, the overtopping events are correctly captured with the approach based on Eq. (17) but the individual overtopping volumes are overestimated (see Fig. B.17 with $c_V = 0.55$). A reason for this overestimation can be the assumption of a constant front velocity during the event resulting in an overestimation of the individual overtopping volumes when no correction is applied.

To compensate for this effect, the mean factor between the volumes from the overtopping box and the approach based on Eq. (17) is computed. This results in a factor of 0.52. In Fig. B.18 the obtained total volumes are compared to those from the overtopping box. This result shows that applying this correction results in a reasonable estimate for the individual overtopping volumes. Almost all the obtained volumes are within a factor 2 of the total volume from the overtopping box.

To show the effect of the applied method to determine the individual overtopping volumes, the number of overtopping events (N_{ov}), the 20% exceedance individual overtopping volume in terms of overtopping events ($V_{20\%,ov}$) and 2% individual overtopping volume in

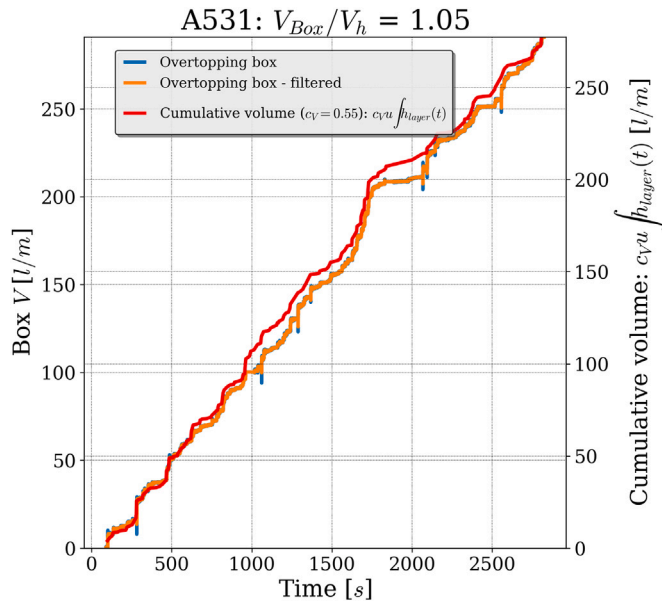


Fig. B.17. Cumulative overtopping volume measured with the overtopping box (left axis, blue and orange line) and obtained from the water layer thickness and Eq. (17) (right axis, red line). Both the raw and filtered signals from the overtopping box are shown (blue and orange lines).

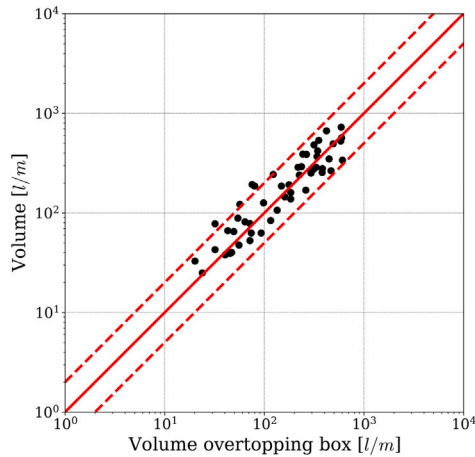


Fig. B.18. Scatter plot of volumes obtained from the overtopping box (x-axis) and the total volume based on Eq. (17) (y-axis). These results are obtained with a correction factor of 0.52. The solid red line represents the 1:1 line and the dashed red lines represent a factor 2.

terms of incident waves ($V_{2\%}$) are compared with the results from the overtopping box in Fig. B.19. This shows that the N_{ov} is underestimated with the volumes obtained from the overtopping box as consecutive events are captured as one event. This results in an overestimation of the individual overtopping volumes with the overtopping box (see Panel B). However, expressed in terms of incident waves these two effects counterbalance each other resulting in similar $V_{2\%}$ between both methods (see panel C).

Appendix C. Log-normal distribution

The log-normal distribution applied in this study is given by,

$$f(V_i) = \frac{1}{sV_i\sqrt{2/\pi}} \exp\left(-\frac{\log(V_i/k_v)^2}{2s^2}\right) \quad (C.1)$$

where s is the shape factor and k_v the scale parameter. Note that other authors used a different definition of the scale parameter. For example, Mares-Nasarre et al. (2024) used the mean of the variable's natural logarithmic (μ_V) to scale the distribution,

$$f(V_i) = \frac{1}{sV_i\sqrt{2/\pi}} \exp\left(-\frac{(\log V_i - \mu_V)^2}{2s^2}\right) \quad (C.2)$$

This means that the μ_V is equal to $\log k_v$.

Appendix D. Effect low-frequency waves on the water layer thickness and front velocities

In Figs. D.20 and D.21 the effects of the low-frequency wave on the water layer thickness and the front velocity are shown for both deep and shallow water. These results show that the conclusions found for the individual overtopping volumes also hold for the front velocity and water layer thickness. In deep water, the largest non-dimensional water layer thickness and front velocities are caused by short waves travelling on the trough of the low-frequency wave, whereas the opposite is true for shallow water. The distribution of the overtopping events is evenly distributed with the mean just left of zero surface elevation for the low-frequency wave in deep water (Panel C) and around zero surface elevation for shallow water (Panel D)

Appendix E. Results for the mean front velocity

See Table E.11.

Appendix F. Confidence intervals for the parameters

For every proposed expression the confidence intervals of the fitted parameters are determined with the bootstrap technique. The proposed expressions (f) have the following form ($h_{2\%}/H_{m0}$, $V_{2\%}/H_{m0}$ and P_{ov}):

$$f = p_1 \exp\left(p_2 \frac{R_c}{H_{m0}} \gamma_f s_{m-1,0,HF}^{p_3}\right) \quad (F.1)$$

or ($u_{2\%}/\sqrt{gh}$),

$$f = p_1 \left(\frac{R_c}{H_{m0}}\right)^{p_2} s_{m-1,0,HF}^{p_3} \quad (F.2)$$

with parameters p_1 , p_2 and p_3 . Given these parameters the 95% confidence intervals of these expressions are shown in Table F.12 presenting the spread of the parameter.

Appendix G. Variable sensitivity

To show how various variables affect the 2% water layer thickness, 2% front velocity, 2% individual overtopping volume and P_{ov} , a machine learning technique is applied to estimate the non-dimensional (extreme) variable ($h_{2\%}/H_{m0}$, \bar{u}/\sqrt{gh} , $V_{2\%}/H_{m0}^2$ and P_{ov}) based on a selection of wave variables. The random forest regressor (see Breiman, 2001 or Geurts et al., 2006 for a description) is applied as a machine learning technique and it is optimized for four different optimization sets of input variables. For each of the optimized models, the feature importance, showing the relevance of the variable for the final estimate, is shown in Table G.13, Table G.14, Tables G.15 and G.16. In each table, the same input variables are applied for the four optimization sets. The first optimization includes all the variables shown in the tables: relative crest height (R_c/H_{m0}), relative water depth (H_{m0}/h), wave asymmetry (A_s), wave skewness (S_k), wave steepness ($s_{m-1,0}$), short-wave steepness ($s_{m-1,0,HF}$), Iribarren number ($\xi_{foreshore}$), relative low-frequency wave height ($H_{m0,LF}/H_{m0}$), relative 2% exceedance wave height ($H_{2\%}/H_{m0}$) and relative setup ($\langle\eta\rangle/H_{m0}$). In the second optimization, the wave skewness and asymmetry are removed showing the results for a set of input variables which can be directly obtained from most numerical spectral models. The third and fourth optimizations show the results for optimization where the properties of the

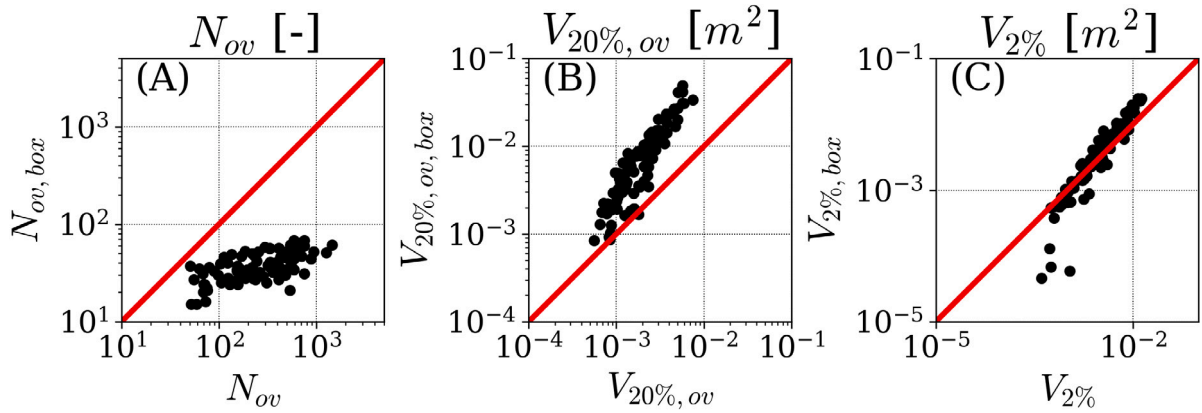


Fig. B.19. Comparison between the number of overtopping events (Panel A, N_{ov}), 20% exceedance individual volume in terms of overtopping events (Panel B, $V_{20\%,ov}$) and 2% individual overtopping volume in terms of incident waves (Panel C, $V_{2\%}$) obtained from the overtopping box and Eq. (17).

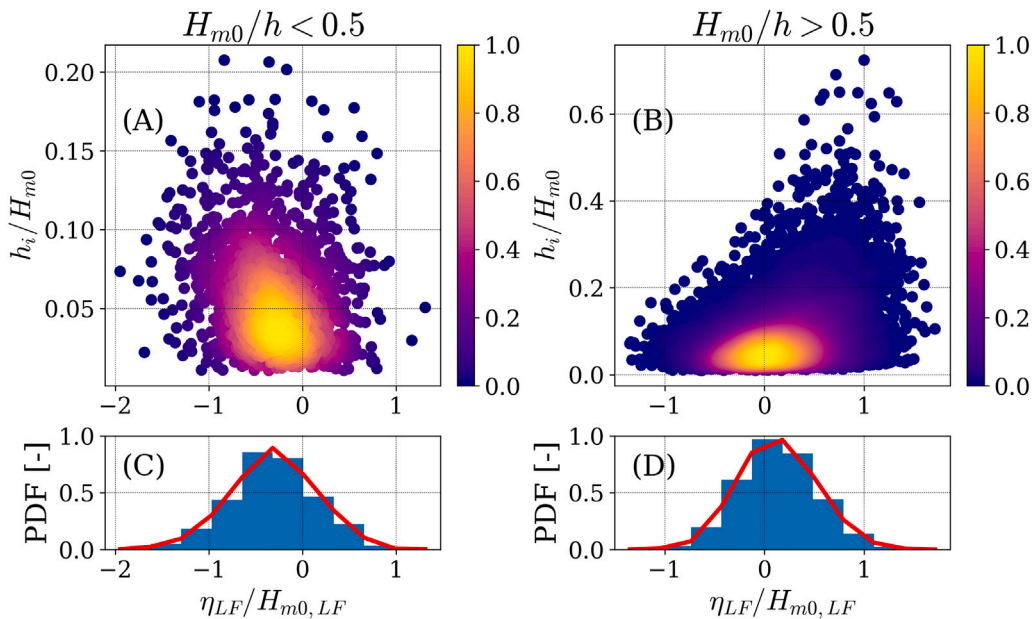


Fig. D.20. Scatter density plot of the non-dimensional water layer thickness as a function of the water surface elevation of the low-frequency wave normalized with the low-frequency wave height (upper panels). The colours of the points indicate the normalized density of the point cloud. The lower panels show the histogram and probability density function of the overtopping events as a function of the surface elevation of the low-frequency wave normalized with the low-frequency wave height. The left panels corresponds to $H_{m0}/h < 0.5$ and the right panels to $H_{m0}/h > 0.5$.

foreshore are removed (water depth in Nr 3 and Iribarren number for Nr 4) because a prediction formulation without foreshore properties is preferred. Such a formulation would be generally applicable as no information on the foreshore is required.

The results differentiate between the various variables, but in general, it can be observed that the relative crest height and short-wave steepness are the most important variables considering optimization Nr 4. Considering the non-dimensional 2% exceedance water layer, the most important variable for optimization Nr 4 is the relative crest height. Remarkable when more variables are available (Nr 1) the short-wave steepness is the most important variable next to the relative water depth. For the mean front velocity, the short-wave steepness and

relative crest height are the most important variables for Optimization Nr 4. The wave asymmetry becomes very important when Nr 1 is considered. For the non-dimensional 2% exceedance volumes, the short-wave steepness is the most important variable for optimization Nr 1 and 4. Lastly, the P_{ov} is mainly related to the relative crest height. For all optimization numbers, the relative crest height is the most important variable.

Note that this method is only applied to get a feeling for the feature importance, but cannot be applied to estimate the variables. The dataset is too limited to apply such a machine-learning method. Moreover, the dataset is not split into a test and training dataset to verify the accuracy of an unseen dataset. The error measures are only included for completeness.

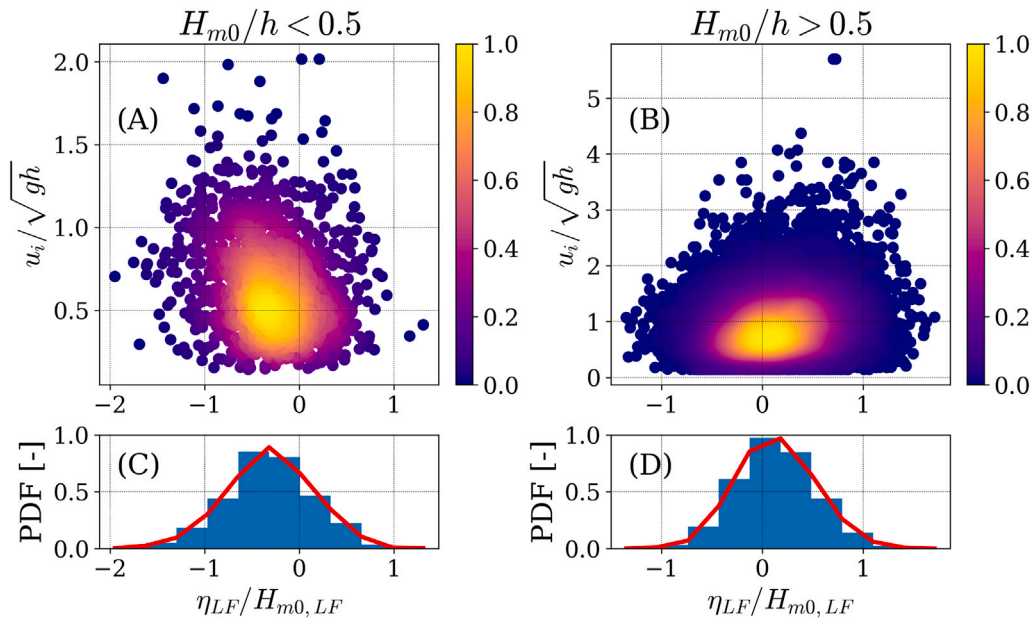


Fig. D.21. Scatter density plot of the non-dimensional front velocity as a function of the water surface elevation of the low-frequency wave normalized with the low-frequency wave height (upper panels). The colours of the points indicate the normalized density of the point cloud. The lower panels show the histogram and probability density function of the overtopping events as a function of the surface elevation of the low-frequency wave normalized with the low-frequency wave height. The left panels corresponds to $H_{m0}/h < 0.5$ and the right panels to $H_{m0}/h > 0.5$.

Table E.11

RMSE and adjusted coefficient of determination for the expression for the mean front velocity at the middle of the crest for various functions. The roughness factor (γ_f) is set to 0.55. Results are obtained for tests with at least 50 overtopping events and a non-dimensional mean overtopping discharge larger than 10^{-5} . The 95% confidence intervals of the coefficients of the proposed expression are given in Table F.12.

| Function | \bar{u}/\sqrt{gh} [-] | RMSE | R^2_{adj} |
|---|-------------------------|------|-------------|
| $\bar{u}/\sqrt{gh} = 1.70 \left(\frac{R_c}{H_{m0}\gamma_f} \right)^{-0.55}$ (E.1) | | 0.25 | 0.16 |
| $\bar{u}/\sqrt{gh} = 0.88 \left(\frac{R_c}{H_{m0}\gamma_f} \right)^{-0.76} s_{m-1,0}^{-0.16}$ (E.2) | | 0.17 | 0.62 |
| ^a $\bar{u}/\sqrt{gh} = 0.51 \left(\frac{R_c}{H_{m0}\gamma_f} \right)^{-0.65} s_{m-1,0,HF}^{-0.32}$ (E.3) | | 0.15 | 0.69 |
| $\bar{u}/\sqrt{gh} = 0.56 \left(\frac{R_c + 0.80H_{m0,LF}}{H_{m0}\gamma_f} \right)^{-0.40} s_{m-1,0,HF}^{-0.21}$ (E.4) | | 0.15 | 0.71 |
| $\bar{u}/\sqrt{gh} = 0.40 \left(\frac{R_c}{H_{2\%}\gamma_f} \right)^{-0.59} s_{m-1,0,HF}^{-0.34}$ (E.5) | | 0.17 | 0.63 |
| $\bar{u}/\sqrt{gh} = 0.52 \left(\frac{R_c - 0.985H_{m0,LF}}{H_{2\%}\gamma_f} \right)^{-0.35} s_{m-1,0,HF}^{-0.19}$ (E.6) | | 0.15 | 0.71 |

^a Eq. E.3 is recommended.

Table F.12

95% confidence interval for the parameters in Eqs. (25), (31), (37) and (45).

| Variable | p_1 | p_2 | p_3 |
|---------------------|-------|-------|--------|
| $h_{2\%}/H_{m0}$ | 5% | 0.52 | -6.25 |
| | 95% | 0.77 | -3.91 |
| $u_{2\%}/\sqrt{gh}$ | 5% | 0.99 | -1.18 |
| | 95% | 1.74 | -0.90 |
| $V_{2\%}/H_{m0}^2$ | 5% | 4.09 | -12.98 |
| | 95% | 8.62 | -7.90 |
| P_{ov} | 5% | 3.91 | -3.85 |
| | 95% | 6.89 | -2.40 |

Table G.13

Feature importance for a random forest regressor with different input wave variables for predicting the non-dimensional water layer thickness. Each column shows the feature importance and the RMSE for a fit with the random forest regressor, with the applied variables changing in each column.

| Optimization Nr | 1 | 2 | 3 | 4 |
|---------------------------------|-------|-------|-------|-------|
| R_c/H_{m0} | 0.18 | 0.19 | 0.22 | 0.31 |
| H_{m0}/h | 0.20 | 0.18 | - | - |
| A_s | 0.09 | - | - | - |
| S_k | 0.04 | - | - | - |
| $s_{m-1,0,HF}$ | 0.29 | 0.32 | 0.35 | 0.56 |
| $s_{m-1,0}$ | 0.01 | 0.02 | 0.03 | 0.03 |
| $s_{m-1,0,foreshore}^z$ | 0.13 | 0.22 | 0.32 | - |
| $H_{m0,LF}/H_{m0}$ | 0.02 | 0.02 | 0.03 | 0.03 |
| $H_{2\%}/H_{m0}$ | 0.01 | 0.02 | 0.02 | 0.03 |
| $\langle \eta \rangle / H_{m0}$ | 0.02 | 0.03 | 0.03 | 0.04 |
| RMSE ($h_{2\%}/H_{m0}$) | 0.011 | 0.010 | 0.011 | 0.011 |
| R^2 ($h_{2\%}/H_{m0}$) | 0.98 | 0.98 | 0.98 | 0.98 |

Table G.14

Feature importance for a random forest regressor with different input wave variables for predicting the non-dimensional front velocity. Each column shows the feature importance and the RMSE for a fit with the random forest regressor, with the applied variables changing in each column.

| Optimization Nr | 1 | 2 | 3 | 4 |
|---------------------------------|------|------|------|------|
| R_c/H_{m0} | 0.32 | 0.31 | 0.29 | 0.57 |
| H_{m0}/h | 0.09 | 0.36 | - | - |
| A_s | 0.04 | - | - | - |
| S_k | 0.04 | - | - | - |
| $s_{m-1,0,HF}$ | 0.02 | 0.01 | 0.04 | 0.14 |
| $s_{m-1,0}$ | 0.03 | 0.04 | 0.03 | 0.10 |
| $s_{m-1,0,foreshore}^z$ | 0.38 | 0.14 | 0.44 | - |
| $H_{m0,LF}/H_{m0}$ | 0.01 | 0.06 | 0.09 | 0.05 |
| $H_{2\%}/H_{m0}$ | 0.02 | 0.06 | 0.06 | 0.05 |
| $\langle \eta \rangle / H_{m0}$ | 0.04 | 0.02 | 0.04 | 0.09 |
| RMSE ($u_{2\%}/\sqrt{gh}$) | 0.15 | 0.17 | 0.14 | 0.18 |
| R^2 ($u_{2\%}/\sqrt{gh}$) | 0.90 | 0.88 | 0.90 | 0.82 |

Table G.15

Feature importance for a random forest regressor with different input wave variables for predicting the non-dimensional 2% exceedance volume. Each column shows the feature importance and the RMSE for a fit with the random forest regressor, with the applied variables changing in each column.

| Optimization Nr | 1 | 2 | 3 | 4 |
|---------------------------------|------|------|------|------|
| R_c/H_{m0} | 0.14 | 0.15 | 0.18 | 0.22 |
| H_{m0}/h | 0.18 | 0.18 | – | – |
| A_s | 0.19 | – | – | – |
| S_k | 0.04 | – | – | – |
| $s_{m-1.0,HF}$ | 0.21 | 0.35 | 0.34 | 0.50 |
| $s_{m-1.0}$ | 0.03 | 0.06 | 0.08 | 0.10 |
| $\xi_{m-1.0,foreshore}$ | 0.14 | 0.16 | 0.27 | – |
| $H_{m0,LF}/H_{m0}$ | 0.02 | 0.03 | 0.05 | 0.06 |
| $H_{2\%}/H_{m0}$ | 0.03 | 0.04 | 0.04 | 0.06 |
| $\langle \eta \rangle / H_{m0}$ | 0.02 | 0.03 | 0.03 | 0.06 |
| RMSLE ($V_{2\%}/H_{m0}^2$) | 0.17 | 0.17 | 0.18 | 0.18 |
| R^2 ($V_{2\%}/H_{m0}^2$) | 0.94 | 0.94 | 0.95 | 0.94 |

Table G.16

Feature importance for a random forest regressor with different input wave variables for predicting the fraction of overtopping waves (P_{ov}). Each column shows the feature importance and the RMSE for a fit with the random forest regressor, with the applied variables changing in each column.

| Optimization Nr | 1 | 2 | 3 | 4 |
|---------------------------------|------|------|------|------|
| R_c/H_{m0} | 0.53 | 0.59 | 0.60 | 0.62 |
| H_{m0}/h | 0.08 | 0.12 | – | – |
| A_s | 0.16 | – | – | – |
| S_k | 0.07 | – | – | – |
| $s_{m-1.0,HF}$ | 0.03 | 0.07 | 0.08 | 0.10 |
| $s_{m-1.0}$ | 0.01 | 0.04 | 0.05 | 0.07 |
| $\xi_{m-1.0,foreshore}$ | 0.04 | 0.05 | 0.10 | – |
| $H_{m0,LF}/H_{m0}$ | 0.02 | 0.04 | 0.06 | 0.09 |
| $H_{2\%}/H_{m0}$ | 0.03 | 0.06 | 0.06 | 0.06 |
| $\langle \eta \rangle / H_{m0}$ | 0.03 | 0.04 | 0.05 | 0.05 |
| RMSLE (P_{ov}) | 0.22 | 0.26 | 0.26 | 0.28 |
| R^2 (P_{ov}) | 0.93 | 0.90 | 0.91 | 0.87 |

Glossary

\bar{u} Mean front velocity [m/s]

α Structure slope [–]

η_{LF} Low-pass band filtered time series [m]

μ_V Mean of the natural logarithmic of the individual overtopping volumes [m²]

γ_f Roughness factor [–]

$\xi_{m-1.0}$ Iribarren number of structure slope based on H_{m0} and $T_{m-1.0}$ [–]

$$\left(\frac{\tan \alpha}{\sqrt{2\pi H_{m0}/(gT_{m-1.0}^2)}} \right)$$

A_s Wave asymmetry [–]

B Crest width [m]

D_{n50} Nominal stone diameter (50th quantile of the stone size distribution) [m]

$H_{2\%}$ Incident 2% exceedance wave height at the toe of the structure [m]

H_{m0} Incident significant wave height at the toe of the structure [m]

$H_{m0,HF}$ Incident high-frequency wave height based on a cutoff-frequency at the toe of the structure [m]

$H_{m0,LF}$ Incident low-frequency wave height based on a cutoff-frequency at the toe of the structure [m]

$H_{m0,deep}$ Offshore incident significant wave height [m]

N_{ov} Number of overtopping waves [–]

P_{ov} Number of overtopping waves divided by the total number of waves [–]

R_c Crest height above still water level (Freeboard) [m]

R_c^* Non-dimensional relative crest height [–] (R_c/H_{m0})

$R_{u2\%}$ 2% exceedance runup level [m]

S_k Wave skewness [–]

$T_{m-1.0}$ Incident spectral period at the structure's toe [s]

$V_{2\%}$ 2% exceedance individual volume in terms of incident waves [m³/m]

V_i Individual overtopping volume [m³/m]

b Shape parameter of the Weibull distribution [–]

$c_{c,h}$ Coefficient for the transformation of the 2% exceedance water layer thickness over the crest [–]

$c_{c,u}$ Coefficient for the transformation of the 2% exceedance front velocity over the crest

c_h Coefficient for the 2% exceedance water layer thickness [–]

c_u Coefficient for the 2% exceedance front velocity [–]

c_v Coefficient for the 2% exceedance individual volume [–]

f_{cutoff} Cutoff frequency [Hz]

f_p Peak frequency [Hz]

g Gravitational acceleration [m/s²]

h Water depth at the toe of the structure [m]

$h_{2\%}$ 2% exceedance water layer thickness in terms of incident waves

h_{crest} Crest level with respect to the flume floor [m]

h_{deep} Offshore water depth [m]

h_i Individual water layer thickness [m]

h_{layer} Water layer thickness [m]

k_v Scale parameter of the log-normal distribution [m³/m for wave volumes]

m Tangent of foreshore slope [–]

q Mean overtopping discharge [m³/s/m]

q^* Non-dimensional mean overtopping discharge [–]

$s_{m-1.0}$ Wave steepness based on the H_{m0} and $T_{m-1.0}$ [–] ($2\pi \frac{H_{m0}}{gT_{m-1.0}^2}$)

$s_{m-1.0,HF}$ Wave steepness based on the $H_{m0,HF}$ and $T_{m-1.0,HF}$ [–]

$$\left(2\pi \frac{H_{m0,HF}}{gT_{m-1.0,HF}^2} \right)$$

$$s_{m-1,0,deep} \text{ Offshore wave steepness based on the } H_{m0,deep} \text{ and } T_{m-1,0,deep} \\ [-] \left(2\pi \frac{H_{m0,deep}}{gT_{m-1,0,deep}^2} \right)$$

$u_{2\%}$ 2% exceedance front velocity in terms of incident waves [m/s]

u_i Individual front velocity [m/s]

z_a Height above still water [m]

Data availability

The data that has been used is confidential.

References

- Bae, H., Yun, K., Yoon, I., Lim, N., 2016. Human stability with respect to overtopping flow on the breakwater. *Int. J. Appl. Eng. Res.*
- Battjes, J.A., Groenendijk, H.W., 2000. Wave height distributions on shallow foreshores. *Coast. Eng.* 40 (3), 161–182. [http://dx.doi.org/10.1016/S0378-3839\(00\)00007-7](http://dx.doi.org/10.1016/S0378-3839(00)00007-7).
- Besley, P., 1998. *Wave overtopping of seawalls, design and assessment manual*.
- Bosman, G., Van der Meer, J., Hoffmans, G., Schüttrumpf, H., Verhagen, H.J., 2009. Individual overtopping events at dikes. In: *Coastal Engineering 2008: (in 5 Volumes)*. World Scientific, pp. 2944–2956. http://dx.doi.org/10.1142/9789814277426_0244.
- Breiman, L., 2001. Random forests. *Mach. Learn.* 45 (1), 5–32. <http://dx.doi.org/10.1023/A:1010933404324>.
- Chen, W., Warmink, J.J., Van Gent, M.R.A., Hulscher, S.J.M.H., 2022. Numerical investigation of the effects of roughness, a berm and oblique waves on wave overtopping processes at dikes. *Appl. Ocean Res.* 118, 102971. <http://dx.doi.org/10.1016/j.apor.2021.102971>.
- Cox, J.C., Machemehl, J., 1986. Overload bore propagation due to an overtopping wave. *J. Waterw. Port Coast. Ocean Eng.* 112 (1), 161–163. [http://dx.doi.org/10.1061/\(ASCE\)0733-950X\(1986\)112:1\(161\)](http://dx.doi.org/10.1061/(ASCE)0733-950X(1986)112:1(161)).
- De Ridder, M.P., Kramer, J., Den Bieman, J.P., Wenneker, I., 2023. Validation and practical application of nonlinear wave decomposition methods for irregular waves. *Coast. Eng.* 183, 104311. <http://dx.doi.org/10.1016/j.coastaleng.2023.104311>.
- De Ridder, M.P., Van Kester, D.C.P., Van Bentem, R., Teng, D.Y.Y., Van Gent, M.R.A., 2024. Wave overtopping discharges at rubble mound structures in shallow water. *Coast. Eng.* 194, 104626. <http://dx.doi.org/10.1016/j.coastaleng.2024.104626>.
- EurOtop, 2018. *Manual on wave overtopping of sea defences and related structures*. URL: www.overtopping-manual.com. In: Van der Meer, J.W., Allsop, N.W.H., Bruce, T., De Rouck, J., Kortenhaus, A., Pullen, T., Schüttrumpf, H., Troch, P., Zanuttigh, B. (Eds.).
- Franco, L., De Gerloni, M., Van der Meer, J.W., 1995. Wave overtopping on vertical and composite breakwaters. In: *Coastal Engineering 1994*. vol. 6349, American Society of Civil Engineers, pp. 1030–1045. <http://dx.doi.org/10.1061/9780784400890.076>.
- Geurts, P., Ernst, D., Wehenkel, L., 2006. Extremely randomized trees. *Mach. Learn.* 63 (1), 3–42. <http://dx.doi.org/10.1007/s10994-006-6226-1>.
- Hasselmann, K., 1962. On the non-linear energy transfer in a gravity-wave spectrum part 1. General theory. *J. Fluid Mech.* 12 (4), 481–500. <http://dx.doi.org/10.1017/S0022112062000373>.
- Herrera, M.P., Gómez-Martín, M.E., Medina, J.R., 2017. Hydraulic stability of rock armors in breaking wave conditions. *Coast. Eng.* 127, 55–67. <http://dx.doi.org/10.1016/j.coastaleng.2017.06.010>.
- Herrera, M.P., Medina, J.R., 2015. Toe berm design for very shallow waters on steep sea bottoms. *Coast. Eng.* 103, 67–77. <http://dx.doi.org/10.1016/j.coastaleng.2015.06.005>.
- Hughes, S.A., Thornton, C.I., Van der Meer, J.W., Scholl, B., 2012. Improvements in describing wave overtopping processes. 1, (33), p. 35.
- Hunt, I.A., 1959. Design of seawalls and breakwaters. *J. Waterw. Harb. Div.* 85 (3), 123–152. <http://dx.doi.org/10.1061/JWHEAU.0000129>.
- Janssen, T.T., Battjes, J.A., Van Dongeren, A.R., 2003. Long waves induced by short-wave groups over a sloping bottom. *J. Geophys. Res.: Oceans* 108 (C8), <http://dx.doi.org/10.1029/2002JC001515>.
- Koosheh, A., Etemad-Shahidi, A., Cartwright, N., Tomlinson, R., Van Gent, M.R.A., 2021. Individual wave overtopping at coastal structures: A critical review and the existing challenges. *Appl. Ocean Res.* 106, 102476. <http://dx.doi.org/10.1016/j.apor.2020.102476>.
- Koosheh, A., Etemad-Shahidi, A., Cartwright, N., Tomlinson, R., Van Gent, M.R.A., 2022. Distribution of individual wave overtopping volumes at rubble mound seawalls. *Coast. Eng.* 177, 104173. <http://dx.doi.org/10.1016/j.coastaleng.2022.104173>.
- Koosheh, A., Etemad-Shahidi, A., Cartwright, N., Tomlinson, R., Van Gent, M.R.A., 2024. Wave overtopping layer thickness on the crest of rubble mound seawalls. *Coast. Eng.* 188, 104441. <http://dx.doi.org/10.1016/j.coastaleng.2023.104441>.
- Longuet-Higgins, M.S., Stewart, R.W., 1962. Radiation stress and mass transport in gravity waves, with application to a surf beat. *J. Fluid Mech.* 13 (4), 481–504. <http://dx.doi.org/10.1017/S0022112062000877>.
- Mares-Nasarré, P., Argente, G., Gómez-Martín, M.E., Medina, J.R., 2019. Overtopping layer thickness and overtopping flow velocity on mound breakwaters. *Coast. Eng.* 154, 103561. <http://dx.doi.org/10.1016/j.coastaleng.2019.103561>.
- Mares-Nasarré, P., Molines, J., Gomez-Martin, M.E., Medina, J.R., 2020. Individual wave overtopping volumes on mound breakwaters in breaking wave conditions and gentle sea bottoms. *Coast. Eng.* 159, 103703. <http://dx.doi.org/10.1016/j.coastaleng.2020.103703>.
- Mares-Nasarré, P., Molines, J., Gómez-Martín, M.E., Medina, J.R., 2021. Explicit neural network-derived formula for overtopping flow on mound breakwaters in depth-limited breaking wave conditions. *Coast. Eng.* 164, 103810. <http://dx.doi.org/10.1016/j.coastaleng.2020.103810>.
- Mares-Nasarré, P., Van Gent, M.R.A., Morales-Nápoles, O., 2024. A copula-based model to describe the uncertainty of overtopping variables on mound breakwaters. *Coast. Eng.* 189, 104483. <http://dx.doi.org/10.1016/j.coastaleng.2024.104483>.
- Molines, J., Herrera, M.P., Gómez-Martín, M.E., Medina, J.R., 2019. Distribution of individual wave overtopping volumes on mound breakwaters. *Coast. Eng.* 149, 15–27. <http://dx.doi.org/10.1016/j.coastaleng.2019.03.006>.
- Nørgaard, J.Q.H., Andersen, T.L., Burcharth, H.F., 2014. Distribution of individual wave overtopping volumes in shallow water wave conditions. *Coast. Eng.* 83, 15–23. <http://dx.doi.org/10.1016/j.coastaleng.2013.09.003>.
- Røge Eldrup, M., Lykke Andersen, T., 2019. Estimation of incident and reflected wave trains in highly nonlinear two-dimensional irregular waves. *J. Waterw. Port Coast. Ocean Eng.* 145 (1), 04018038. [http://dx.doi.org/10.1061/\(ASCE\)WW.1943-5460.0000497](http://dx.doi.org/10.1061/(ASCE)WW.1943-5460.0000497).
- Schüttrumpf, H., Möller, J., Oumeraci, H., 2003. Overtopping flow parameters on the inner slope of seadikes. In: *Coastal Engineering 2002: Solving Coastal Conundrums*. World Scientific, pp. 2116–2127. http://dx.doi.org/10.1142/9789812791306_0178.
- Schüttrumpf, H., Van Gent, M.R.A., 2003. Wave overtopping at seadikes. In: *Coastal Structures 2003*. American Society of Civil Engineers, pp. 431–443. [http://dx.doi.org/10.1061/40733\(147\)36](http://dx.doi.org/10.1061/40733(147)36).
- TAW, 2002. *Wave Run-Up and Wave Overtopping at Dikes. Technical Report, Technical Advisory Committee for flood defence in the Netherlands (TAW) Delft*.
- Van der Meer, J.W., Hardeman, B., Steendam, G.-J., Schüttrumpf, H., Verheij, H., 2010. Flow depths and velocities at crest and landward slope of a dike, in theory and with the wave overtopping simulator. 1, (32), *Citeseer*, p. 10, URL: <http://resolver.tudelft.nl/uuid:e14f478c-dd62-42e3-9191-aeef909e0d95>,
- Van Gent, M.R.A., 1999. Physical model investigations on coastal structures with shallow foreshores: 2D model tests with single and double-peaked wave energy spectra. URL: <http://resolver.tudelft.nl/uuid:1b4729de-2e86-4b8a-98d5-48d8e07d5902>.
- Van Gent, M.R.A., 2001. Wave runup on dikes with shallow foreshores. *J. Waterw. Port Coast. Ocean Eng.* 127 (5), 254–262. [http://dx.doi.org/10.1061/\(ASCE\)0733-950X\(2001\)127:5\(254\)](http://dx.doi.org/10.1061/(ASCE)0733-950X(2001)127:5(254)).
- Van Gent, M.R.A., 2002. Low-exceedance wave overtopping events. URL: <http://resolver.tudelft.nl/uuid:e71289dd-f6aa-471e-856c-832071a83753>.
- Van Gent, M.R.A., 2003. Wave overtopping events at dikes. In: *Coastal Engineering 2002: Solving Coastal Conundrums*. World Scientific, pp. 2203–2215. http://dx.doi.org/10.1142/9789812791306_0185.
- Van Gent, M.R.A., 2021. Influence of oblique wave attack on wave overtopping at caisson breakwaters with sea and swell conditions. *Coast. Eng.* 164, 103834. <http://dx.doi.org/10.1016/j.coastaleng.2020.103834>.
- Van Gent, M.R.A., 2023. *Wave Overtopping at Dikes and Breakwaters under Oblique Wave Attack*. (37), Coastal Engineering Research Council, <http://dx.doi.org/10.9753/icce.v37.papers.5>, 5–5.
- Victor, L., Van der Meer, J.W., Troch, P., 2012. Probability distribution of individual wave overtopping volumes for smooth impermeable steep slopes with low crest freeboards. *Coast. Eng.* 64, 87–101. <http://dx.doi.org/10.1016/j.coastaleng.2012.01.003>.
- Zanuttigh, B., Van der Meer, J., Bruce, T., Hughes, S., 2014. Statistical characterisation of extreme overtopping wave volumes. In: *From Sea to Shore—Meeting the Challenges of the Sea: (Coasts, Marine Structures and Breakwaters 2013)*. ICE Publishing, pp. 442–451.